ELSEVIER

Applied Soft Computing

SUFEMO: A superpixel based fuzzy image segmentation method for COVID-19 radiological image elucidation

Check for updates

Shouvik Chakraborty *, Kalyani Mali

Department of Computer Science and Engineering, University of Kalyani, India

ARTICLE INFO

ABSTRACT

COVID-19 causes an ongoing worldwide pandemic situation. The non-discovery of specialized drugs and/or any other kind of medicines makes the situation worse. Early diagnosis of this disease will be certainly helpful to start the treatment early and also to bring down the dire spread of this highly infectious virus. This article describes the proposed novel unsupervised segmentation method to segment the radiological image samples of the chest area that are accumulated from the COVID-19 infected patients. The proposed approach is helpful for physicians, medical technologists, and other related experts in the quick and early diagnosis of COVID-19 infection. The proposed approach will be the SUFEMO (SUperpixel based Fuzzy Electromagnetism-like Optimization). This approach is developed depending on some well-known theories like the Electromagnetism-like optimization algorithm, the type-2 fuzzy logic, and the superpixels. The proposed approach brings down the processing burden that is required to deal with a considerably large amount of spatial information by assimilating the notion of the superpixel. In this work, the EMO approach is modified by utilizing the type 2 fuzzy framework. The EMO approach updates the cluster centers without using the cluster center updation equation. This approach is independent of the choice of the initial cluster centers. To decrease the related computational overhead of handling a lot of spatial data, a novel superpixel-based approach is proposed in which the noise-sensitiveness of the watershed-based superpixel formation approach is dealt with by computing the nearby minima from the gradient image. Also, to take advantage of the superpixels, the fuzzy objective function is modified.

The proposed approach was evaluated using both qualitatively and quantitatively using 310 chest CT scan images that are gathered from various sources. Four standard cluster validity indices are taken into consideration to quantify the results. It is observed that the proposed approach gives better performance compared to some of the state-of-the-art approaches in terms of both qualitative and quantitative outcomes. On average, the proposed approach attains Davies–Bouldin index value of 1.812008792, Xie–Beni index value of 1.683281, Dunn index value 2.588595748, and β index value 3.142069236 for 5 clusters. Apart from this, the proposed approach is also found to be superior with regard to the rate of convergence. Rigorous experiments prove the effectiveness of the proposed approach and establish the real-life applicability of the proposed method for the initial filtering of the COVID-19 patients.

1. Introduction

Artificial intelligence and computer vision can make many difficult tasks easy with the help of automated and intelligent frameworks. These methods are capable to analyze and discover various complex datasets without any help from humans. Moreover, the automated systems often surpass human experts in finding various complex patterns and hidden relationships among the data points in a dataset. These features make this domain

lucrative and attract researchers to apply it in many real-life problem-solving scenarios. Machine learning belongs to the artificial intelligence domain and has many applications in different domains. It is an emerging field of research and continuous development effort can be observed in the literature [1–3]. One of the earlier applications of machine learning is noticed in the checker games in 1959 and it replaces the humans to play the game [4]. The modern machine learning systems can be categorized in two ways: supervised learning and unsupervised learning. Supervised systems demand some training data to acquire some knowledge about the underlying dataset and can learn continuously from the available annotated data. In contrast, unsupervised methods do not use any ground truth data for learning. Instead of that, this

* Corresponding author.
E-mail addresses: shouvikchakraborty51@gmail.com (S. Chakraborty), kalyanimali1992@gmail.com (K. Mali).

type of system can explore the dataset and find some relationships or patterns from the constituting data points without any supervision. This type of system is useful where a significantly large amount of ground truth data (with appropriate annotations) is not available. Among various applications, biomedical image processing and its interpretation is one of the major domains of research where machine learning and computer vision-based systems are frequently used [5–7]. Machine learning empowered computer vision-based systems can be exploited as a helping hand for the physicians to assess the condition of a patient [8,9].

Radiology is an important domain of biomedical imaging that helps in understanding the state of the various internal organs in a non-invasive manner. This work exploits the advantages of the radiological image analysis to get a hint about the initial attack of the COVID-19 using the chest CT images. Early detection of this virus can help reduce the drastic spread and also helpful in taking precautionary measures. The proposed approach adopts the concept of superpixels to bring down the processing cost that are incurred by the processing of a huge amount of spatial information. The proposed approach also modifies the fuzzy objective function to exploit the advantages of the superpixels. The proposed approach can never replace the traditional gold standards to detect the presence of the COVID-19 virus but, can help in the initial isolation of the suspects and also in early treatment.

1.1. Motivation

Machine learning empowered and computer vision-based automated systems can be highly useful in keen exploring and interpreting radiological images and to help physicians in preparing accurate and precise reports within the stipulated amount of time [10–12]. Not only the radiological image interpretation, but the automated systems can also help the radiologists in different ways like determining the radiation level, image enhancement, parameter adjustment of the image acquisition device, assessment of different parameters to maintain the quality, etc. [5,13, 14]. The Corona Virus Disease 2019 which is also known as the COVID-19, creates a pandemic scenario worldwide. It is highly infectious and there is no such specialized medicine is available to date. More than 505 million (505,817,953) total confirmed cases are reported and more than 6 million (6,213,876) total deaths are reported in the world, so the mortality rate is near about 1.23% due to this virus [15] as in April 2022 (up to 5:47 pm CEST, 22nd April 2022). The infectious nature of this disease can be easily understood by observing the number of infected countries. At present, 216 countries are suffering from this virus. Early screening can prevent this virus from getting spread and it is one of the necessary safety measures for survival under the present pandemic scenario. Although the RT-PCR test has already proven its effectiveness in detecting the presence of COVID-19 virus, the chest CT (Computerized Tomography) scans can be used to explore some early signs of the COVID-19 infection [16], and therefore, radiological image analysis is considered as a promising way to battle against the spread of the COVID-19 infection [17]. Radiological images cannot be used for the final decision-making process regarding the infection because some studies show that some confirmed COVID-19 positive patients cannot be properly diagnosed with the radiological images [18,19] but, it is useful in the early isolation of a susceptible person from other healthy persons. It can be helpful to restrict the community spread by early diagnosis. Ground truth segmented images for the COVID-19 infected chest CT scan images with appropriate annotations are not available to a large extent. Chest CT scans are useful in this context and also recommended in [20] for the initial screening process. Some apposite features like crazy paving, ground-glass

opacities, etc. [21,22] can be observed in the chest CT scan images that are collected from the COVID-19 infected patients and these features are reported in Table 1 [23,24]. Motivated from this, a new biomedical image segmentation approach is developed namely SUFEMO (SUperpixel based Fuzzy Electromagnetism-like Optimization) for easy segmentation of the radiological images by optimizing the superpixel based fuzzy objective function. The type-2 fuzzy logic-based clustering approach is integrated into the proposed work to generate better clusters compared to the crisp clustering methods. Automated and efficient analysis of the radiological images is possible using the proposed method that makes the screening process easier. So, computer-aided diagnostic systems can be an effective weapon to restrict the spread of the COVID-19 disease.

Hence, the following are the key advantages of this approach:

1. Efficient handling of huge spatial information is possible.
2. Cluster centers can be automatically determined without depending on the choice of initial cluster centers.
3. The fuzzy objective function is modified to exploit the advantages of superpixels.
4. There is no need to use any manual delineations for segmentation purposes.

1.2. An outline of the theoretical and practical contributions

This article proposes a novel approach to process and interpret investigate CT examination pictures for early screening of COVID-19. It is the extension of the FEMO [25] approach where the concept of modified superpixel approach is incorporated to reduce the overall computational burden. This contribution can go about as a helping hand for the doctors and furthermore supportive to counter the drastic spread of this infection without relying upon the pre-annotated dataset and it makes the proposed approach useful and appropriate to be applied in various real-life scenarios. In this work, the EMO approach is altered utilizing the type 2 fuzzy framework. The EMO approach updates the cluster centers without using cluster center updation equation. This approach is independent of the choice of the initial cluster centers. To decrease the related computational overhead of handling a lot of spatial data, a novel superpixel-based approach is proposed in which the noise-sensitiveness of the watershed-based superpixel formation approach is dealt with by computing the nearby minima from the gradient image. Also, to take advantage of the superpixels, the fuzzy cost function is changed as needs are. These are the significant contributions to the state-of-the-art literatures from both practical and theoretical aspects. It can be helpful to restrict the community spread by early diagnosis. Ground truth segmented images for the COVID-19 infected chest CT scan images with appropriate annotations are not available to a large extent.

It can be noted that, these features are illustrated in this section to describe how the radiological images can be used in early diagnosis purposes. Although the proposed method can effectively perform the segmentation job, the SUFEMO approach is cannot distinguish these features. Therefore, the rest of the article does not talk about these features.

The organization of the remaining article is as follows: Section 2 is dedicated to some of the related works of literature. The methodology is described in Section 3 where some preliminary concepts are discussed in brief and the proposed approach is discussed in detail. Section 4 presents the experimental outcomes and their analysis. Section 5 concludes the article.

Table 1

Some significant findings in the CT scans of the chest regions that are collected from COVID-19 positive patients [23].

Name of the observed property in the chest CT scan image of the chest region of the COVID-19 infected patients	Explanation/Meaning	Percentage of the observed samples
Ground-glass opacities (GGO)	It refers to a portion of the lungs with increased attenuation.	100%
Multilobe and posterior involvement	Impact on both lobes and posterior area.	93%
Bilateral pneumonia	It means that pneumonia has attacked both lungs i.e., double pneumonia.	91%
Sub-segmental vessel enlargement (>3 mm)	It is marked as vessel diameter greater than 3 mm	89%

2. Related works

With the increasing rate of infection, many researchers are trying to find some automated solutions to efficiently diagnose the presence of this virus from the radiological images and prevent the drastic spread. In this section, some of the recent approaches are discussed briefly.

A novel CT scan image segmentation technique is proposed in [26] and this approach is applied to segment the CT images that are collected from the COVID-19 infected patients. This method is a supervised one where the model can learn the segmentation delineations from the supplied annotations. The experimental outcomes show that this approach can deliver significant performance in finding affected regions from the CT images of the chest regions. An automated CT image segmentation approach is proposed in [27] and this approach is also applied on the CT images of the chest area of the COVID-19 infected patients. This approach is an unsupervised approach that can precisely detect and segment the infected region from the chest CT scans. This approach basically a multilevel thresholding scheme that optimizes Kapur's entropy. The segmented outcomes are validated with the manual delineations and the performance of this approach is found to be satisfactory for clinical applications. A deep learning approach-based abnormality detection approach from chest CT scan images is proposed in [28]. This approach consists of lesion detection, segmentation. The location of the abnormalities is trained with the help of 14, 435 participants and tested with the samples collected from 96 patients from China. The comparison with the manual delineations proves the effectiveness and strength of this approach. A deep learning approach is proposed in [29] that automate the diagnosis process of the COVID-19 using the X-ray images. This approach obtains 98.08% accuracy for the binary classification i.e., COVID vs normal, and 87.02% accuracy for multi-class classification. This approach also produces the heatmap that is helpful for the physicians in locating the COVID-19 infection from the X-ray images. A deep learning approach is proposed in [30] that can process the volumetric chest CT scans to find the COVID-19 infection. 4536 number of test images are involved in this work and it is observed that this approach can efficiently differentiate between COVID-19 and society-obtained pneumonia and some other lung-related issues.

An automated deep learning approach is designed in [31] to determine the traces of abnormalities in the chest region. The experiments are carried out with 126 patients infected with COVID-19 and it is observed that method can efficiently determine various areas with opacifications from the chest CT scans. A combined segmentation and classification approach for the chest CT scans is presented in [32]. This approach is known as a dual-branch combination network. This work also proposes a lesion attention component to enhance the sensitivity that is helpful to segment small lesions that is helpful in COVID-19 detection. This approach proves to be efficient with a smaller amount of sample datasets. This approach obtains 96.74% accuracy while acting on the internal image dataset and obtains 92.87% accuracy while acting on the external validation collection.

An unsupervised approach is proposed in [33] that can be employed to perform the segmentation of the infected lung areas using the lung CT volumes. This approach is based on image inpainting and representation learning techniques. This approach uses a preprocessing approach to discard the high-intensity regions to avoid incorrect segmentation. This approach initially segments the pulmonary blood vessels and the image inpainting approach is applied on the segmented pulmonary blood vessels. After that the infected lung regions are segmented. Obtained results are quite encouraging and demonstrates the strength of this method. This approach is successfully secured 0.394 mutual information score. An automated framework to diagnose COVID-19 infection is proposed in [34]. This approach can diagnose the COVID-19 disease from the CT scan images and X-ray images of the chest area. This work developed a ideational structure for automated analysis of these images and this approach exploits the advantages of the transfer learning technique. The classification process is implemented with the help of the ResNet-18 model. The obtained outcomes illustrate that this approach can secure 95% accuracy. A novel retinal blood vessel segmentation approach is proposed in [35]. In this work, a joint model of a guided filter and a matched filter is recommended for upgrading unusual retinal pictures containing poor vessel contrasts. To obtain all data from a picture precisely is one of the significant elements and prime objective of image enhancement phase. This strategy applies a quick guided filter and a matched filter for obtaining further enhanced method for vessel extraction. This suggested strategy was applied and the performance is tested on DRIVE and CHASE_DB1 datasets and accomplished encouraging accuracy of 0.9613 and 0.960, respectively. A correlation relationship learning mechanism (CLM) is proposed in [36] to detect brain tumor using CT scan images. This work is based on deep neural network models that consolidates convolutional neural network (CNN) with traditional architecture. The additional neural network assists CNN with tracking down the most satisfactory filters for pooling and convolution layers. This approach is proven to reach around 96% accuracy, and around 95% precision. Another technique for the super-resolution recreation of a single character image in light of the wavelet neural network is proposed in [37]. Integrated with the pinhole imaging technique and camera self-calibration, image acquisition in IoT is accomplished. An image degradation model was laid out to recreate the degradation phenomena of an ideal high-resolution image with a low-resolution image. Wavelet threshold denoising strategy is utilized to eliminate the commotion in a solitary character image and further develop the counter interference execution of the technique. The wavelet neural network reflection approach is utilized to remake the single frame feature image and enhance the image resolution. In the entire trial, the accuracy of this technique can be kept up at 80%~90%.

A comprehensive survey on this topic can be discovered in [38, 39]. A brief summary of some of the related state-of-the-art approaches is given in Table 2.

From the cutting-edge writing, it tends to be seen that a large portion of the methodologies are utilizing supervised or semi-supervised learning. As talked about before, acquiring manual

Table 2

A quick run-through of the related methods.

Reference	Category	Real-life deployment locations (NA indicates not available)	Important points	Future scopes
Chen et al. [40]	Supervised approach	Renmin Hospital, Wuhan University, China	• It is a deep learning-based approach that is used to determine the presence of COVID-19 by analyzing high-resolution chest CT scans. The focal area is selected by exploiting the UNet++ framework. • Experimental results show that this approach can achieve 95.24% accuracy that is quite remarkable. • Apart from this, this work also achieves 100% sensitivity, and 93.55% specificity that shows the effectiveness of this work.	• Some variants of the UNet++ model can be applied to test the performance. • This approach can be applied and evaluated to different types of images.
Wang et al. [41]	Supervised approach	NA	• This work exploits the advantages of the modified transfer learning to analyze CT scan images and bring out some useful features. • This approach can work with an accuracy of 79.3%, a specificity of 83.00%, and a sensitivity of 67.00%.	• Some hybrid transfer learning approaches can be evaluated and compared with this approach. • Different set of images can be used to check the performance of the proposed approach. • Attempts can be made to improve the accuracy and other parameters.
Butt et al. [42]	Supervised approach	NA	• A three-dimensional CNN-based segmentation method is developed for effective segmentation of the infected areas of the chest using the CT images. • This work uses multiple CNNs for classification purposes. • The probability of the infection is computed with the help of the Bayesian function. • This approach can work with 98.2% sensitivity and 92.2% specificity.	• Attempts can be made to improve the feature representation. • Various image datasets can be explored. • Different functions can be tested that replace the Bayesian function.
Xu et al. [43]	Supervised approach	NA	• Two 3D CNN-based classification methods are hybridized and a novel classification approach is presented. • This approach is applied and tested to classify three different types of lung infections namely COVID-19, Influenza, and not any specific infection category. • It can perform with an overall accuracy of 86.7%.	• Attempts can be made to improve the accuracy of the system. • This approach can be further enhanced to mine fine features from the biomedical images to effectively classify different other classes. • This approach can be designed to solve multi-class classification problem and can be tested for different types of images and also for different classes of images.
Jin et al. [44]	Supervised approach	16 different hospitals in China	• A Transfer learning-supported framework is designed that can effectively analyze CT images. • This approach exploits the ResNet-50 as the underlying model. • The segmentation work is performed with the help of the 3D UNet++ model. • This approach can achieve a sensitivity of 97.4% and a specificity of 92.2%.	• Same approach can be exploited and evaluated after incorporating various other standard models. • Some other models can also be taken under consideration to perform the segmentation task. • This approach can also be extended to work on different datasets.
Wang et al. [45]	Weakly-supervised approach	NA	• This is a lung lesion detection approach that analyzes the chest CT chest using a weakly supervised model. • This approach uses a UNet architecture as a backbone segmentation model. • The possibility of the COVID-19 infection is analyzed with a 3D deep neural architecture.	• The proposed approach can also be used to develop a new segmentation model by incorporating different architectures and segmentation backbone. • This problem can be extended to solve the multi-class classification problem. • This approach some modifications of this approach can be applied to the biomedical images of different modalities.

outlines or getting division veils from domain specialists is very troublesome. Hence, in this work, an original unaided methodology is suggested that can help in the early discovery of the COVID-19 disease from the chest CT images. This methodology, using any and all means, does not rely on any manual outlines or ground truth information. This methodology can be basically carried out in various emergency clinics or demonstrative establishments for an underlying screening reason that aides in taking careful steps that can limit the spread of this infection.

3. Method and materials

3.1. A brief description of the electromagnetism-like optimization

Electromagnetism-like optimization (EMO) strategy is a meta-heuristic optimization technique and it is created by Birbil and Fang [52]. The EMO technique can decide the global optima of a solution space by imitating the attraction–repulsion conduct of the charged particles. Here, every arrangement is considered as

Table 2 (*continued*).

Mohammed et al. [46]	Weakly-supervised approach	NA	• It is weakly-supervised that can perform the segmentation job with the help of the segmentation mask. • This method is known as ResNext+ and it can extract spatial features using spatial and channel attention. • This method proves to be efficient enough and can achieve a precision rate 81.9% and F1 score value 81.4%.	• This problem can also be extended to the multiclass classification problem. • This approach can also be applied to some benchmark image segmentation datasets.
Laradji et al. [47]	Weakly-supervised approach	NA	• This work is a feebly regulated methodology that utilizes a few focuses to check the tainted regions that can viably discover the depictions naturally. • This plan is known as point checking and it ends up being sufficiently productive to be applied, in actuality, applications.	• The point checking method may incorporate gradient information efficiently. • This approach can be further hybridized with some metaheuristic approaches.
Laradji et al. [48]	Weakly-supervised	NA	• This is a feebly regulated methodology that can mark the CT pictures successfully and in a timebound style. • This work is essentially a functioning learning approach. • By investing 7% annotation effort, this methodology can perform with 90% productivity contrasted with the totally clarified dataset.	• This approach can be further extended to reduce the existing annotation overheads. • Heterogeneous datasets may be closely investigated to apply this approach in interdisciplinary applications.
Gozes et al. [49]	Supervised approach	NA	• This methodology can robotize the investigation interaction of the chest CT pictures utilizing a 2D profound CNN. • The Resnet-50 model is utilized as the foundation of the characterization model while the U-net engineering manages the division issue. • This technique can work with 98.2% sensitivity and 92.2% specificity.	• This approach can be further investigated and may be deployed in real-life robotic disease investigation. • The foundation model can be further updated to enhance the quality of the investigation. • The effectiveness of this approach can be further investigated on some standard image datasets.
Chakraborty et al. [50]	Unsupervised approach	NA	• A morphological recreation activity-based chest CT picture division approach is proposed in this work. • The edge content-based organized network approach is utilized to decide the ideal organizing components. • The trial results show that this methodology beats many cutting-edge approaches as far as some standard assessment measurements. • On average this approach achieves 307.1888625 MSE value, 23.7246505 PSNR value, and 0.831718459 SSIM value.	• This approach can be further extended to compare the obtained results with some other standard approaches like dice coefficient, accuracy etc. so that the performance of this approach can be assessed with respect to some manually delineated images. • The edge content-based network can be further modified to incorporate point-wise region information.
Han et al. [51]	Semi-Supervised approach	NA	• This methodology is a semi-supervised methodology that analyzes the COVID-19 infection from the chest CT examine pictures. • This methodology utilizes both marked and unlabeled information to improve exactness. • This methodology can successfully separate between normal pneumonia and COVID-19 contamination with 97.32% accuracy, 0.9971 sensitivity, 0.9598 specificity, and 0.9326 PPV. • The comparative outcomes prove its superiority.	• This approach can be applied to different modalities of the biomedical images. • Multi-class classification problem can also be addressed. • Dependency on the marked label can be reduced

the charged molecule and the measure of the charge is controlled by the fitness value. The process begins by initializing the population randomly. In the next phase, the local optima are located by applying a local search technique. This step can incorporate any standard methods like hill-climbing [53], gradient descent method [54], etc. to perform the local search. The superposition principle [25,55] is applied in the third step to determine the force exerted by the particles. The amount of the force can be calculated by the magnitude of the charge of a particle and the distance between two particles as illustrated in Fig. 1. In this diagram, $\vec{F}_{ij}$ denotes the force which is exerted by a particle p_i on another particle p_j. In EMO, a better particle attracts other particles toward it and a worse particle repulse other. In this diagram, the particle p_1 is repulsed by the particle p_3 and attracted by the particle p_2. The particle p_1 is experiencing the resultant force $\vec{F}_1$ which can be expressed as $\vec{F}_1 = \vec{F}_{31} + \vec{F}_{21}$. A detailed discussion on force calculation and particle shifting can be found in [56–58].
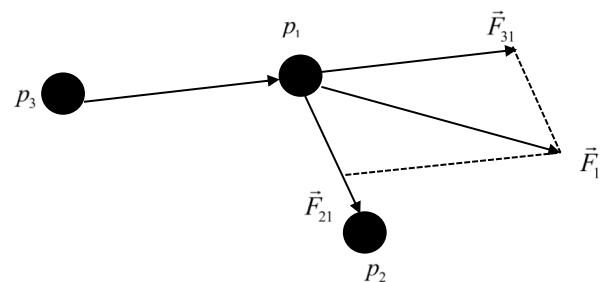

Fig. 1. Illustration of the superposition principle which is used to compute the cumulative force in EMO algorithm.

The calculated force is utilized in the following stage to move the particles and the last three stages are rehashed until the end models are satisfied. The end condition can be set by the interest of the issue or relying upon the exactness required. Eq. (1) shows

---

Algorithm 1: The electromagnetism-like optimization (EMO) procedure

---

Inputs: The size of the initial population sz. The upper bound of the global iteration counter and the local iteration counter $gIterationCnt$ and the $lIterationCnt$ respectively. The controlling parameter of the local search $\tau \in [0,1]$.

Output: Computed optimal result(s)

1: $population \leftarrow initializePop(sz)$: Initialize the population of size sz.

2: $fit \leftarrow calculateFitness(population)$: determine the fitness value of individual solution in the population.

3: Repeat the following steps while termination criteria is not satisfied

    a. $lSearch(lIterationCnt, \tau)$: execute the local search

    b. $force \leftarrow findForce(fit)$: compute the force

    c. $shiftParticles(force)$: shift the particles based on the computed force.

End Repeat

---

the generalized form of a non-linear optimization problem with a box constraint that can be solved by the EMO method.

$$\max f(q), \quad q = (q_1, q_2, q_3, \ldots \ldots, q_n) \in \mathbb{R}^n \ subject \ to \ q \in Q \quad (1)$$

In this equation, $f : \mathbb{R}^n \rightarrow \mathbb{R}$ represents a non-linear function and $Q = \{q \in \mathbb{R}^n | low_j \leq q_j \leq high_j, j = 1, 2, 3, \ldots \ldots, n\}$ is a region which is bounded by the lower and the upper bounds low_j and $high_j$ respectively. Algorithm 1 describes the basic EMO approach briefly. The function $initializePop(sz)$ is used to initialize the initial population of size sz. After initializing the population, it is essential to compute the fitness of each individual. The fitness calculation procedure is executed by the $calculateFitness()$ function. The local search operation as described earlier is executed by the $lSearch()$ function. In EMO approach the movement of the particles is carried out by computing the exerted force due to the other particles as described in Fig. 1. $findForce()$ approach is used to determine the exerted force by each particle due to other particles that are present in the population. The execute the movement of the particles, $shiftParticles()$ function comes into picture.

3.2. Fuzzy type-2 C-means clustering

Fuzzy grouping frameworks are for all intents and purposes valuable in various events where the crisp clustering methods do not exactly measure up well. There are a few uses of fuzzy clustering frameworks that can be found to take care of different practical issues [59,60]. The fuzzy clustering frameworks have the adaptability of permitting a solitary pixel to be a piece of the various groups at the same time with some level of membership and, the absolute amount of the multitude of degrees for a specific point should be 1. The squared error objective function work for the fuzzy C-means grouping framework is given in equation 2 and the cluster centers can be refreshed by applying Eq. (4). This equation serves as the objective function for the fuzzy C-means clustering algorithm.

$$Obj_\phi = \sum_{i=1}^{nPnt} \sum_{j=1}^{nCen} \mu_{ij}^\phi \left\| x_i - c_j \right\|^2, \ where \ 1 \leq \phi < \infty \quad (2)$$

μ_{ij}^ϕ denotes the membership value of the point x_i to the jth cluster and ϕ denotes the fuzzifier. The degree of membership

can be calculated using Eq. (3). As examined before, the amount of the participation esteems for a specific point should be 1 i.e. $\sum_{j=1}^{nCen} \mu_{ij} = 1 \ for \ i = 1, 2, 3, \ldots \ldots, nPnt$. Here, $nPnt$ and $nCen$ denotes the number of available data points and the number of cluster centers.

$$\mu_{ij} = \frac{1}{\sum_{s=1}^{nCen} \left(\frac{\| x_i - c_j \|}{\| x_i - c_s \|} \right)^{\frac{2}{\phi-1}}} \quad (3)$$

$$c_j = \frac{\sum_{i=1}^{nPnt} \mu_{ij}^\phi x_i}{\sum_{i=1}^{nPnt} \mu_{ij}^\phi} \quad (4)$$

The type-1 fuzzy frameworks experience the ill effects of commotion and relative participation esteems which is unsafe to the fragmented result. This issue can be settled by applying the type-2 fuzzy framework where the uncertainty of a point is high if the membership value is low as well as the other way around [61–63]. In addition, the participation esteems are considered as weights. The significant benefits of type-2 fuzzy framework based clustering approach are referenced beneath [64,65]:

    a. Uncertainties can be efficiently modeled and a point with lesser uncertainty has a higher impact than a point with higher uncertainty.

    b. In the viable situation, some more sensible yields can be created by the type-2 fuzzy clustering framework contrasted with the type-1 fuzzy clustering frameworks.

    c. Higher noise invulnerability can be accomplished.

The modified membership value ω_{ij} in type-2 fuzzy clustering system can be computed using Eqs. (5) and, (6) can be used to update the cluster centers. The proposed approach uses meta-heuristics (as described in the next subsection) to update the cluster centers by optimizing the proposed superpixel-based fuzzy objective function and the subtleties of the proposed approach are examined in the following section. Algorithm 2 describes the fuzzy type-2 clustering method.

$$\omega_{ij} = \mu_{ij} - \frac{1 - \mu_{ij}}{2} \quad (5)$$

$$\hat{c}_j = \frac{\sum_{i=1}^{nPnt} \omega_{ij}^\phi x_i}{\sum_{i=1}^{nPnt} \omega_{ij}^\phi} \quad (6)$$

Algorithm 2: Type-2 fuzzy C-means clustering

Input: The dataset and the cluster count $nCen$ where, $2 \leq nCen \leq nPnt$

Output: Optimal cluster centers

1: Randomly assign the degree of membership to each available point and also randomly choose the cluster centers.
2: Set a small threshold value κ.
3: Apply equation 6 to determine the updated cluster centers.
4: Apply equation 2 to determine the fitness value.
5: Check if $improvement \geq \kappa$ then

     a. Apply equation 5 to determine the value of the type-2 fuzzy participation ω_{ij}.

     b. Goto step 2.
    end if
6: Return the best cluster centers.

3.3. Proposed SUFEMO approach

With the progressions in the field of biomedical imaging, the nature of image obtaining devices is getting worked on day by day. Biomedical picture acquisition innovation is currently profoundly evolved and it is feasible to catch high-quality pictures of different modalities. The mechanized examination of these pictures gets troublesome because of the expanding measure of spatial data with the expanding number of pixels. To deal with this issue effectively, a superpixel [66,67] based novel image segmentation segmentation strategy is proposed in this work. Superpixels can address the spatial data in a more calculation cordial way contrasted with the adjoining window approach. On account of the adjoining window approach, some little windows which are of comparable shape and size are thought of. The concept of superpixel is used on many occasions before performing the segmentation [68] and several approaches are using which the superpixels of an image can be computed [69–71]. Superpixels can be of regular sizes and shapes or irregular shapes and sizes. The SLIC [70] method produces regular superpixels whereas, the Mean shift [69] and the watershed [71] method produce irregular superpixels. Irregular superpixels are more useful compared to the regular superpixels. Albeit the mean shift and the watershed strategies can deliver irregular superpixels, the mean shift technique is all the more oftentimes utilized contrasted with the watershed strategy in light of the fact that the watershed approach is touchy to noise. The mean shift strategy is intricate and computationally more costly than the watershed approach and furthermore subject to certain boundaries like bandwidth, the smallest space of a region, and so forth.

A watershed approach based computationally less expensive (contrasted with the mean shift technique), and boundary autonomous strategy is proposed in this work. The watershed approach works by deciding the area minima from the gradient images. [72]. The gradient image comparing to an actual image is processed utilizing the technique proposed in [73]. The watershed-based superpixel strategy can prompt the over-segmentation issue because of the noise affectability and in this way the final segmentation result can be incorrect and it is exorbitant according to the diagnostic point of view on the grounds that some unacceptable conclusion can cause unseemly treatment. The commotion can be dealt with by thinking about just the significant gradient information. Morphological erosion (ψ) and dilation (ζ) operations (mathematically expressed in Eqs. (9) and (10) respectively) based reconstruction operations (Ω^ψ and Ω^ζ) [74] are helpful to consider only important gradient information, and these are given in Eqs. (7) and (8) respectively.

It is worth mentioning in this context that Eqs. (9) and (10) seems to be recursive. The internal term of the r.h.s. of Eq. (9) and Eq. (10) i.e., $\psi^{k-1}\left(\tilde{I}\right)$ and $\zeta^{k-1}\left(\tilde{I}\right)$ can be computed using $\psi_I^1\left(\tilde{I}\right) = \psi\left(\tilde{I}\right) \vee I$ and $\zeta_I^1\left(\tilde{I}\right) = \zeta\left(\tilde{I}\right) \wedge I$ respectively on the first phase. Values can be replaced in the main equation and these procedures are repeated until all pixels are processed. The details about the recursive approach to perform erosion transform and dilation transform can be found in [75].

The original image and the marker image are represented by I, and $\tilde{I}$ respectively and can be expressed by Eqs. (13) and (14) where υ denotes the structuring element. The original image and the marker image are processed with the help of the morphological erosion and dilation operations using the structuring element υ. The morphological erosion and dilation operations are two popular operators in digital image processing and they occur in pair due to their dual nature.

$$\Omega_I^\psi\left(\tilde{I}\right) = \psi_I^k\left(\tilde{I}\right) \tag{7}$$

$$\Omega_I^\zeta\left(\tilde{I}\right) = \zeta_I^k\left(\tilde{I}\right) \tag{8}$$

Morphological erosion-based reconstruction operation Ω^ψ demands to be $\tilde{I} \geq I$ and the morphological dilation-based reconstruction operation Ω^ζ demands to be $\tilde{I} \leq I$. Morphological erosion (ψ) and dilation (ζ) operations are mathematically expressed in Eqs. (9) and (10) respectively. Morphological dilation operation increases the size of the object by adding some pixels in the boundary region. In contrast to that the morphological erosion operation decreases the size of the object by removing some pixels from the boundary area.

$$\psi_I^k(I) = \psi\left(\psi^{k-1}\left(\tilde{I}\right)\right) \vee I \tag{9}$$

$$\zeta_I^k(I) = \zeta\left(\zeta^{k-1}\left(\tilde{I}\right)\right) \wedge I \tag{10}$$

In these equations, two operators $\vee$ and $\wedge$ denotes the point wise maximum and the minimum values. Eqs. (11) and (12) can be used for the morphological reconstruction purpose using the morphological opening (o) and closing (ς) operations respectively. These two activities can manage the noisy images more effectively contrasted with the erosion and the dilation tasks. Consequently, morphological opening and closing activities are liked over the morphological erosion and the dilation jobs. Morphological opening operation is an erosion operation followed by a dilation operation. Whereas the morphological closing operation is a dilation operation followed by an erosion.

$$\Omega_I^o\left(\tilde{I}\right) = \Omega^\zeta\left(\Omega^\psi\right) \tag{11}$$

$$\Omega_I^\varsigma \left(\tilde{I} \right) = \Omega^\psi \left(\Omega^\varsigma \right) \tag{12}$$

The over-segmentation issue which can be brought about by the watershed approach can be kept away from by recognizing the nearby minima from the gradient image utilizing the Ω^o or Ω^ς. The dilation and erosion based marker image can be formed using Eqs. (13) and (14) respectively.

$$\tilde{I} = \zeta_\upsilon \left(I \right) \tag{13}$$

$$\tilde{I} = \psi_\upsilon \left(I \right) \tag{14}$$

The impact of the structuring element is very important in generating the segmented output [72,76,77]. It can be noted that the smaller structuring elements can lead to the under-segmentation and larger structuring elements can lead to the over-segmentation. It tends to be handily perceived that the size of the structuring elements might change contingent upon the picture i.e., for all pictures, it is preposterous to expect to apply the equivalent structuring elements. This dependency can be removed by considering the gradient images which are produced by more than one structuring element of different sizes. These pictures are consolidated and the pointwise largest values are calculated to save the significant edge related information and to dispose of the nearby minima. The count of the structuring elements can be controlled relying upon the scope of the controlling parameter χ e.g., the width of the square structuring element, the sweep of the disc structuring element, and so forth. The altered form of Eq. (11) is given in Eq. (15) where χ_{low} and χ_{high} means the lower and the upper limits of the controlling parameter χ respectively. Figs. 2 and 3 [78] delineate the impact of the size of the circle and square structuring element separately on the superpixel image. The quantity of superpixels is slowly diminishing with the expanding size of the structuring element and it can be perceived in Fig. 4(a) and (b).

$$\tilde{\Omega}_I^o \left(\tilde{I}, \chi_{low}, \chi_{high} \right) = \max \left\{ \Omega_I^o \left(\tilde{I} \right)_{\upsilon_{\chi_{low}}}, \Omega_I^o \left(\tilde{I} \right)_{\upsilon_{\chi_{low}+1}}, \right.$$
$$\left. \Omega_I^o \left(\tilde{I} \right)_{\upsilon_{\chi_{low}+2}}, \ldots, \Omega_I^o \left(\tilde{I} \right)_{\upsilon_{\chi_{high}}} \right\} \tag{15}$$

In Eq. (15), $\chi_{low} \le \chi \le \chi_{high}$ and $\left[\chi_{low}, \chi_{high} \right] \in \mathbb{N}^+$. On the off chance that the lower bound is minuscule, the final segmented outcome will comprise of tiny locales, and assuming it is very high, there is an opportunity to lose significant edge data [6, 72]. In this equation, $\tilde{\Omega}^o$ uses multi-scale structuring elements to produce multiple reconstructed images. These reconstructed gradient images are useful in generating good quality gradient images. Here, good quality means these images remove most of the local minima and preserves essential edge information. Pointwise maxims of the recreated gradient images are needed to be figured in advance to eliminate the nearby minima and hold significant edge features. Here, the value of the threshold plays a crucial role and, in this work, it is selected in an experimental manner. However, this can be an interesting work for the future to automatically decide the threshold value depending on the context. However, this work may sometime face (very rare conditions) some performance issues due to the manual tuning of this parameter. The upper bound can be chosen relying upon the picture however, it will be more reasonable to set a tiny threshold ε that can be used as the error rate and depending on this value, the upper bound can be decided as expressed below (Eq. (16)):

$$\left\{ \tilde{\Omega}_I^o \left(\tilde{I}, \chi_{low}, \chi_{high} \right) - \tilde{\Omega}_I^o \left(\tilde{I}, \chi_{low}, \chi_{high} + 1 \right) \right\} \le \varepsilon \tag{16}$$

If the threshold value ε is high then the error rate will be high yet a more modest upper bound will be accomplished as well as the other way around i.e., the value of the upper bound is

Table 3
The controlling variables and their selected values.

Controlling variable	Selected value
Population size sz	20
$gIterationCnt$	350
$lIterationCnt$	50
The local search parameter τ	0.005
Number of clusters	Subjective

contrarily corresponding to the threshold value. The increasing value of the χ_{high} increases the computational overhead. Thus, the computational intricacy can be diminished by bringing about the higher error rate. So, the threshold value should be carefully selected.

In this work, the fuzzy type-2 clustering system is used to classify these superpixels. To execute the classification, the fuzzy objective function which is given in Eq. (2) should be altered to take advantage of the major benefits of the superpixels. The superpixels are the assortment of pixels and each superpixel is represented by an agent pixel esteem σ_m that is possible to obtain using Eq. (17). In this equation, nPx_m denotes the pixel count in the mth region R_m and px_z is a pixel in the area R_m. The modified fuzzy objective function is given in Eq. (18) where nR represents the number of regions. So, a single pixel is represented by a superpixel to reduce the computational overhead. This equation is derived from the actual fuzzy objective function with a little modification to incorporate the advantages of the superpixel . This equation treats a superpixel as a unit. The membership value μ_{mj} can be determined using Eq. (19).

$$\sigma_m = \frac{1}{nPx_m} \sum_{z \in R_m} px_z \tag{17}$$

$$Obj_\phi = \sum_{m=1}^{nR} \sum_{j=1}^{nCen} nPx_m \mu_{mj}^\phi \left\| \sigma_m - c_j \right\|^2, \; where \; 1 \le \phi < \infty \tag{18}$$

$$\mu_{mj} = \frac{1}{\sum_{q=1}^{nCen} \left(\frac{\left\| \sigma_m - c_j \right\|}{\left\| \sigma_m - c_q \right\|} \right)^{\frac{2}{\phi-1}}} \tag{19}$$

In this work, the type-2 fuzzy framework is adjusted for the benefits it which are talked about in the past segment. The type-2 participation value can be determined utilizing Eq. (20) and it is gotten from Eq. (19).

$$\eta_{mj} = \mu_{mj} - \frac{1 - \mu_{mj}}{2} \tag{20}$$

The fuzzy cluster center updation equation is not required because the proposed method employs the EMO algorithm to update the cluster centers. The controlling parameters and their chosen values are mentioned in Table 2. The flow diagram of the SUFEMO approach is given in Fig. 5. Algorithm 3 illustrates the proposed SUFEMO method. Some controlling parameters of the proposed framework are tabulated in Table 3. The overall flows of the proposed approach can be visually understood from Fig. 6.

As discussed earlier, the procedure starts by randomly initializing some points that form the population and this number is denoted by sz. The points are thought to be uniformly distributed in between the middle of the lower and the upper limits. The value of the objective function is required to be computed for every point. The greatest number of iterations that are permitted to be executed is signified by $gIterationCnt$. The parameter $lIterationCnt$ is used to control the iterations during the execution of the local search procedure. τ is the controlling parameter for the local search process. This parameter is used to compute the
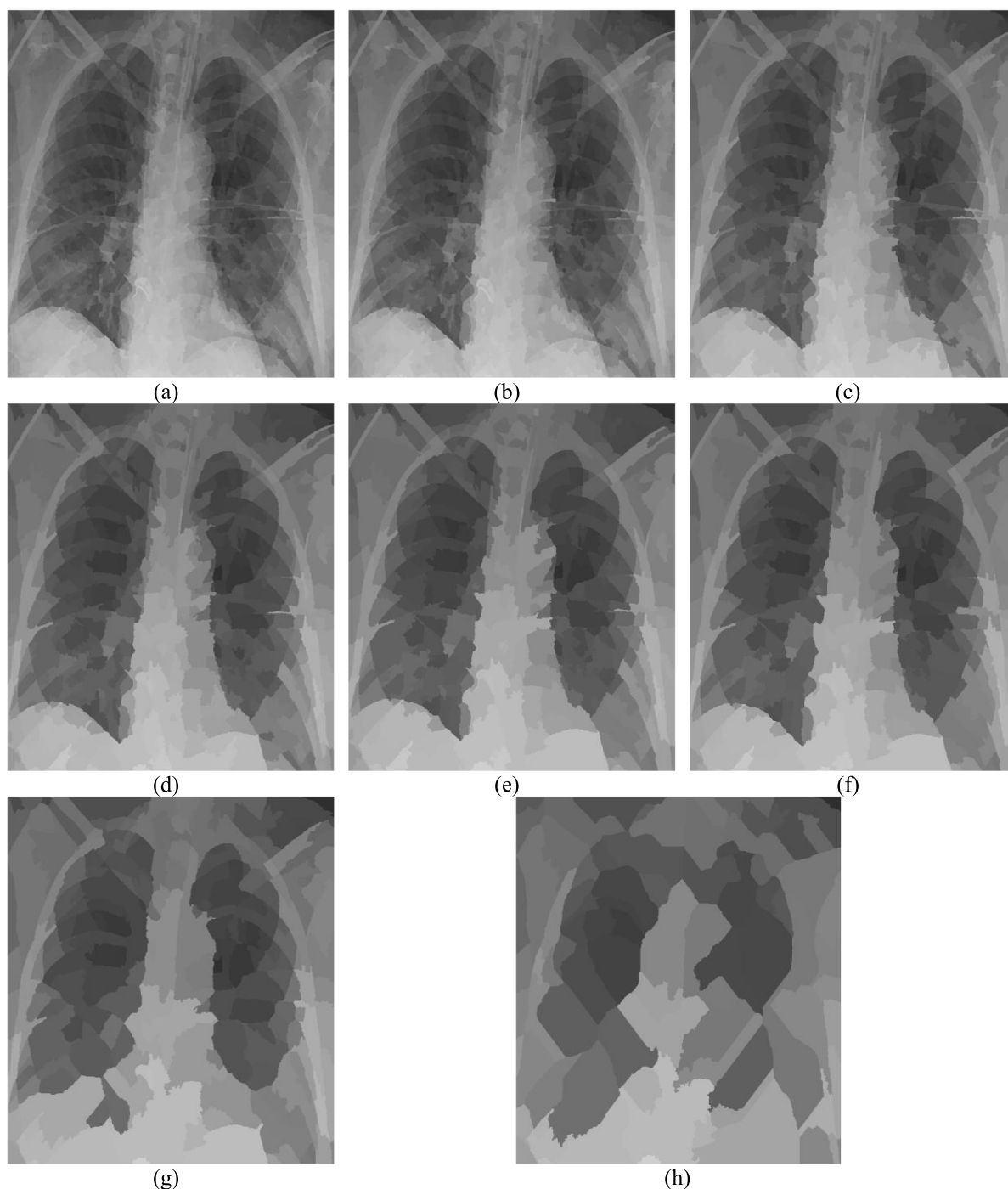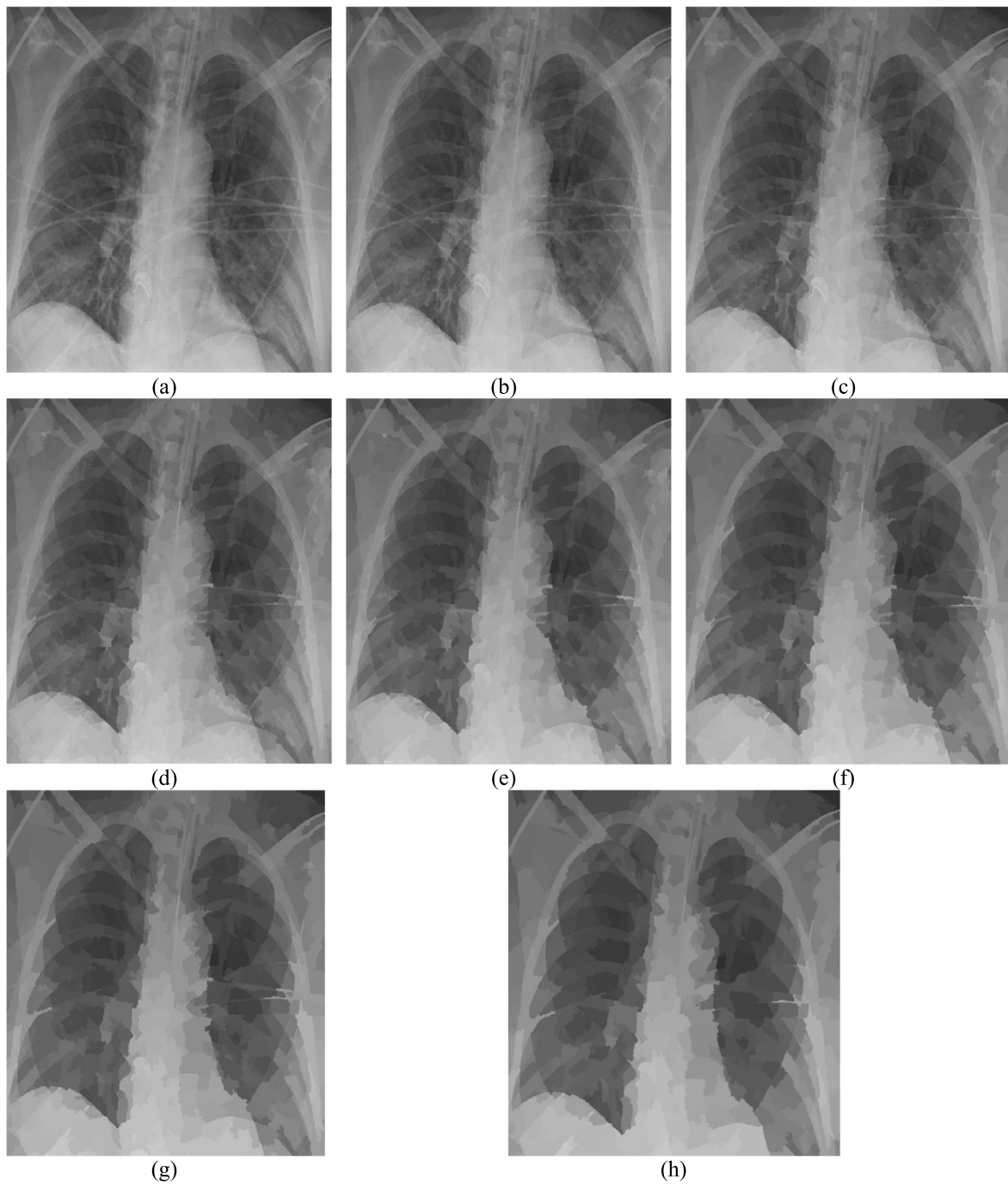
Fig. 2. Illustration of the impact of the diverse sizes of the structuring elements (a)–(h) the superpixel pictures delivered by applying the circle structuring elements of size 3 to 10 separately.

feasible step length [52] for the neighborhood search method. The local search system is not subject to gradient information. The local search system utilizes a line search way to deal with search all coordinate points in the inquiry space. In the wake of executing the local search system, the force experienced by different particles is determined, and relying upon these forces, the movement of the particles happens for the local search proce-dure. The local search procedure is not dependent on the gradient information. The local search procedure employs a line search approach to search all coordinate points in the search space. After executing the local search procedure, the force exerted by

various particles is calculated, and depending on these forces, the movement of the particles takes place.

It is worth mentioning here that these values are determined based on experimental outcomes. These variables are physically tuned in such a manner with the goal that ideal test outcomes can be accomplished. However, there is a scope to incorporate some automated approaches to tune these parameters depending on the underlying image and it will be certainly an interesting future work.

Actually, the cluster centers are randomly selected but clusters are not. Clusters are determined using the proposed approach

Fig. 3. Illustration of the impact of the diverse sizes of the structuring elements (a)–(h) the superpixel pictures delivered by applying the square structuring elements of size 3 to 10 separately.
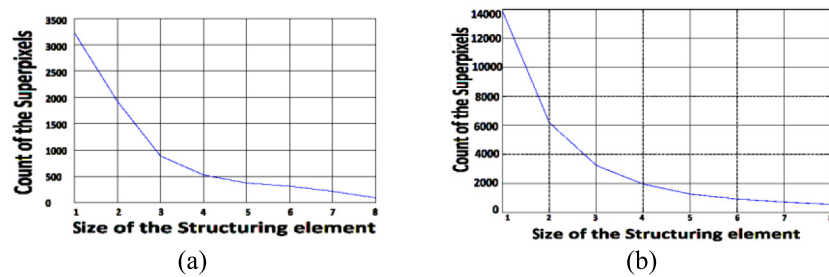
Fig. 4. Graphical portrayal of the size of the organizing component and the number of superpixels (in *X*-axis (1,2,….,8), the size of the structuring element is plotted and in *Y*-axis (0,500,100,….,3500) the count of the superpixels is plotted) (a) Circle Structuring element, (b) Square Structuring element.
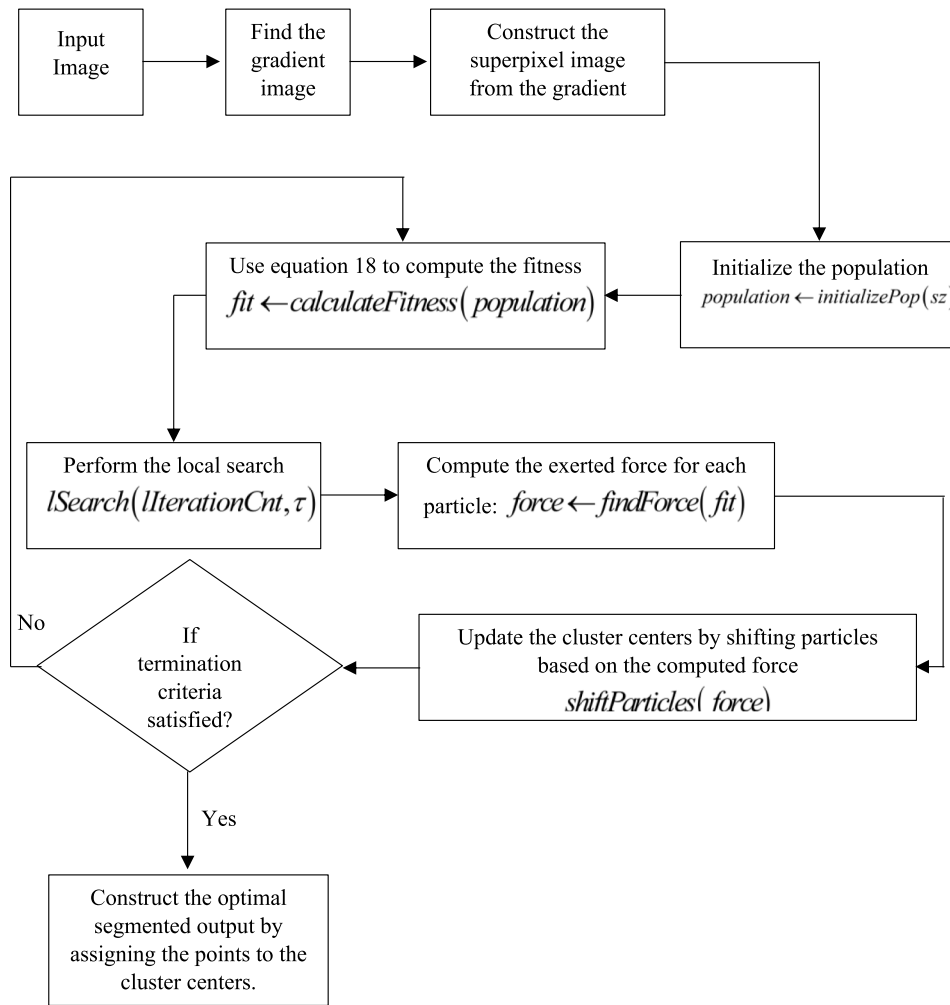
Fig. 5. The flow diagram of the proposed SUFEMO technique.
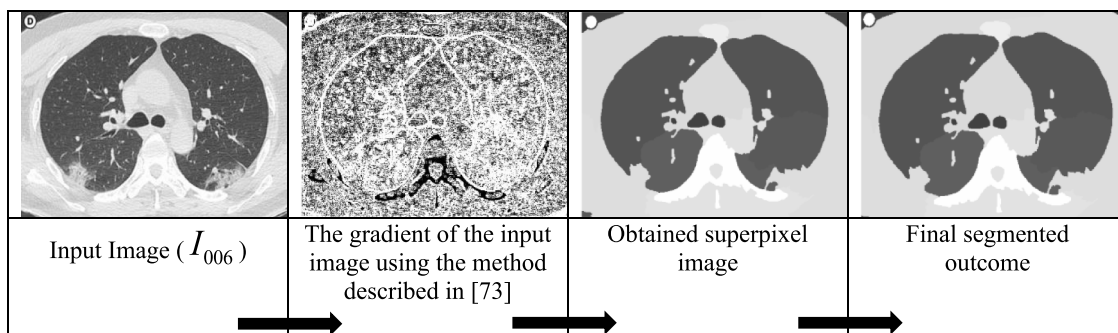
Fig. 6. Stepwise graphical explanation of the proposed approach along with detailed flow diagram.

as discussed in algorithm 3. There are no dependencies on the choice of initial cluster centers (that is also a strength of the proposed algorithm). The proposed fuzzy approach guides the initial set of cluster centers and helps to achieve optimal cluster centers and optimal clustering outcomes as well (that is further validated using some standard cluster validity indices. However, the proposed approach is not capable of determining the number of clusters automatically. The hybridization of the superpixel concept is highly beneficial in reducing spatial information and computational complexity.

As given in Algorithm 3, the proposed SUFEMO approach starts by discovering the gradient image by applying the technique as talked about in [73]. The gradient information is useful in determining the superpixel image using the modified superpixel computation approach as already discussed and Eqs. (11) and (12) are used to determine the superpixel. The cluster centers can be randomly initialized using $CC_i = \sigma_{low} + random\,(0,1)\,(\sigma_{high} - \sigma_{low})$ where σ_{high} and σ_{low} are the lowest and the highest values corresponding to the representative point of a superpixel. After computation of the superpixel, the type-2 fuzzy membership is assigned to the superpixels using Eq. (20). After generating the initial population, the fuzzy optimization process will be repeated for *gIterationCnt* times where, *gIterationCnt* count denotes the global iteration count. The parameter *cntItr* can be considered

---

Algorithm 3: The proposed SUFEMO algorithm

Input: Image to be analyzed and the initial values of the controlling parameters

Output: Segmented output corresponding to the input image

1: Find the gradient image corresponding to the input image using the technique illustrated in [73].
2: Determine the superpixel image by applying equations 11 and 12.
3: Randomly assign the initial values to the cluster centers $CC_i = \sigma_{low} + random(0,1)(\sigma_{high} - \sigma_{low})$

where σ_{high} and σ_{low} are the highest and the lowest values of the representative point corresponding to a superpixel respectively.
4: Apply equation 20 to initialize the fuzzy type-2 participation degree to the superpixels.
5: $population \leftarrow initializePop(sz)$: Initialize the population of size SZ.
6: $cntItr \leftarrow 1$
7: Repeat until $cntItr > gIterationCnt$
8:     $fit \leftarrow calculateFitness(population)$: find the fitness value of each solution in the population.
9:     $lSearch(lIterationCnt, \tau)$: perform the local search
10:     $force \leftarrow findForce(fit)$: compute the force.
11:     $shiftParticles(force)$: shift the particles based on the computed force and update the cluster centers.
12:     $cntItr \leftarrow cntItr + 1$
    end until
13: Consider the optimal cluster centers to build the final segmented outcome.
14: Return the region delineated image.

---

as the loop counter that keeps track of how many times the optimization process is already repeated. It can be noted that, the parameter *lIterationCnt* in step 9, is the local iteration count that is required for the local optimization process. Inside the optimization loop, at first, the fitness values of each member of the population are computed and after that, a local optimization process is executed. The movement of the particles is dependent on the resultant force exerted by the particles. After the necessary movement of the particles, the cluster centers are refreshed likewise. When the upgraded cluster centers are acquired, the portioned yield can be developed by allocating the superpixels to their closest cluster centers.

4. Results of the simulation

The proposed SUFEMO strategy is tried on the CT scan images which are gathered from the COVID-19 positive patients. Ground truth fragmented pictures are not generally accessible for these pictures for the early screening reason and consequently the principal objective of this proposed SUFEMO strategy is to give a vigorous and helpful method of screening by breaking down the biomedical pictures so the presumed patients can be disconnected to battle the spread of this profoundly irresistible illness. RT-PCR test can be performed later on for affirmation. Four cluster validity indices are utilized to assess the proposed approach quantitatively which are portrayed later in this segment.

4.1. Illustration of the dataset

The proposed approach is used to segment 310 CT scan images that are randomly selected which are obtained from different countries of the world [79,80]. Fig. 7 gives a brief overview of the 10 test images out of the 300 CT scan images under test. The test images are given in Fig. 7 (see Table 4).

4.2. Validity indices

The proposed SUFEMO technique is assessed utilizing four notable validity indices which are talked about in this subsection. These indices are useful in to assess and look at the clustering approach quantitatively.

i. **Davies–Bouldin index (*DBIndex*):** The Davies–Bouldin file is a habitually utilized quantitative cluster legitimacy measure that figures the proportion of the intra-cluster and inter-cluster distances [91]. Thus, the lowest index value is wanted to deliver a decent clustering outcome. Eq. (21) can be utilized to find the value of it where *c* represents the count of the clusters and $f \neq m$, $1 \leq f \leq c$.

$$DBIndex = \frac{1}{c} \sum_{f=1}^{c} \max \left(\frac{d_w(a_f) + d_w(a_m)}{d_b(a_f, a_m)} \right) \quad (21)$$

ii. **Xie–Beni index (*XBIndex*):** The proportion between the smallness and the partition of the clusters is estimated by this famous fuzzy cluster assessment index. The value of this index can be determined using Eq. (22) [92]. Good clustering results will produce a lower value of this index.

$$XBIndex = \frac{\sum_{p=1}^{c} \sum_{q=1}^{n} U_{pq}^2 \left\| V_p - X_q \right\|^2}{d_{\min} \left\| V_p - V_q \right\|^2} \quad (22)$$

iii. **Dunn index (*DI_n*):** The inter-cluster distance $dist(c_i, c_j)$ and the mean distance between the pair of clusters Ψ_k [93] controls the worth of this index and it can be determined utilizing Eq. (23). A larger value demonstrates better clustering results.

$$DI_n = \min_{1 \leq i \leq n} \left(\min_{1 \leq j \leq n, j \neq i} \left(\frac{dist(c_i, c_j)}{\max_{1 \leq k \leq m} \psi_k} \right) \right) \quad (23)$$
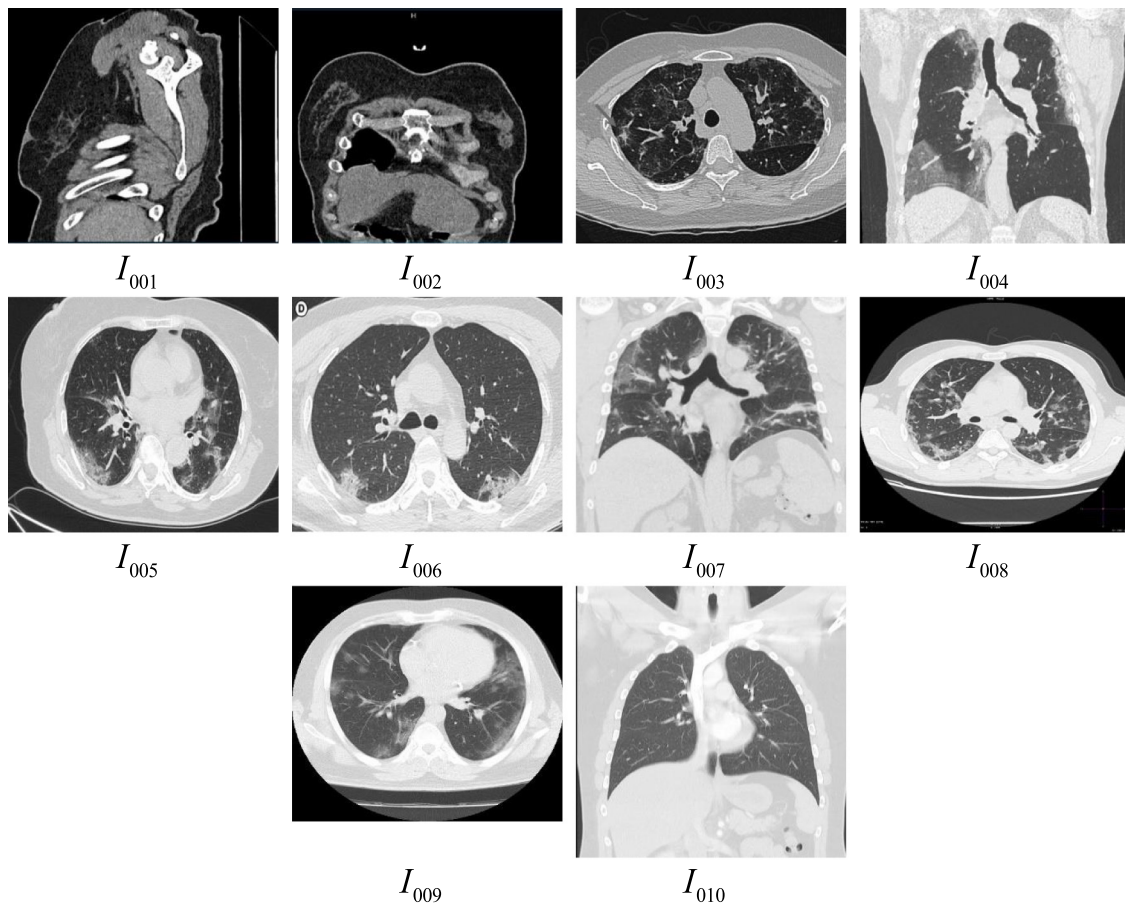
Fig. 7. Some sample test images.

iv. $\boldsymbol{\beta}$ **index**: The proportion of the complete variation and the intra-cluster variation is calculated to determine this index value [94] and Eq. (24) can be utilized to determine the value of the β index. Here, px_m denotes the pixel count in the mth cluster, I_{ml} denotes the pixel intensity, and $x_m = \frac{1}{px_m} \sum_{x=1}^{px_m} I_{xm}$. Good clustering output will produce higher value of the β index.

$$\beta = \frac{\sum_{m=1}^{c} \sum_{l=1}^{px_m} (I_{ml} - x)^2}{\sum_{m=1}^{c} \sum_{l=1}^{px_m} (I_{ml} - x_m)^2} \tag{24}$$

4.3. Experimental results

This subsection is devoted to the report and analysis of the experimental outcomes. It is worth focusing on here that all trials are performed utilizing MatLab R2014a (windows platform) in a computational setup comprising of an Intel i3 processor (1.8 GHz) and 4 GB of primary memory. To assess the proposed approach both subjective and quantitative methodologies are thought of. To comprehend the presentation of a recently evolved approach, it is consistently crucial to compare it with cutting edge approaches like beam Ant Colony Optimization [95], adaptive Particle Swarm Optimization [96], efficient Genetic Algorithm [97] and the modified Cuckoo Search (MCS) method [98]. Figure I_{001} is used for the comparative study and the segmented outcomes are presented in Fig. 8. This experiment is carried out for four different cluster counts. Despite the fact that it is truly challenging to comprehend the performance of the proposed method from the segmented images simply because of the shortfall of any ground truth depictions still, some essence of the performance of various calculations can be acquired. Fig. 8 portrays that

the proposed approach functions admirably concerning different methodologies. The segmented result for the remainder of the pictures, which are acquired utilizing the proposed SUFEMO technique with the distinctive number of clusters is accounted for in Fig. 9. Nonetheless, the quantitative examination is additionally performed to have a nearby gander at the presentation of the proposed SUFEMO technique. Four diverse cluster validity indices i.e., **DBIndex**, **XBIndex**, **DI$_n$** and β index is used for the evaluation purposes. The quantitative outcomes that are generated utilizing various approaches for different number of clusters are accounted for in Table 5 for the **DBIndex**, **XBIndex**, **DI$_n$** and β index.

It can be noticed that a few values are featured in boldface to demonstrate the best-obtained results. Toward the end of each table, average values for every one of the four group validity parameters more than 310 test pictures are accounted for. The proposed approach accomplishes 1.421301735, 1.812008792, 1.587189337, 1.502481616 value of the *DBIndex* for 3, 5, 7, and 9 clusters respectively and outperforms other approaches. Again, the proposed SUFEMO approach achieves 1.628119075, 1.697662119, 2.246409944, 2.310486157 value of the **XBIndex** for 3, 5, 7, and 9 clusters respectively and outperforms other approaches. Similarly, for the **DI$_n$**, the proposed approach achieves 2.584698504, 2.588595748, 2.350004016, 2.868974087for 3, 5, 7, and 9 clusters respectively and outperforms other approaches for 3 and 5 number of clusters but marginally outperformed by the MCS approach for the 7 and 9 number of clusters. Now, for the β index the proposed approach achieves 2.830809221, 3.142069236, 3.790172244, 2.993016698 for 3, 5, 7, and 9 clusters respectively and outperforms other approaches for 3 and 5 number of clusters but outperformed by the MCS approach for the 7 and 9 number of clusters. From this examination, it tends to be seen that the
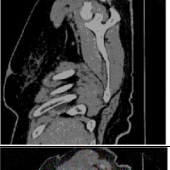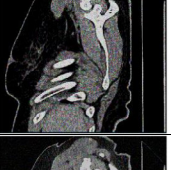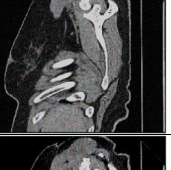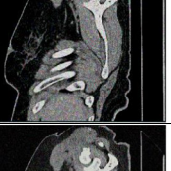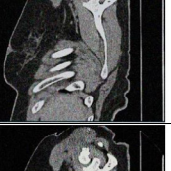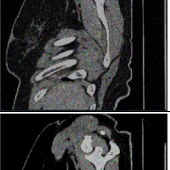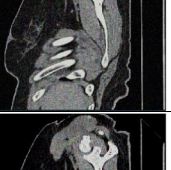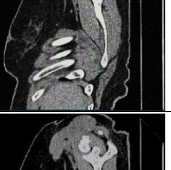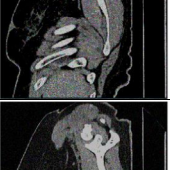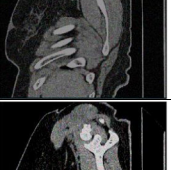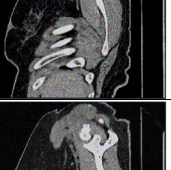
Algorithm	Count of the clusters			
	3	5	7	9
efficient GA [97]				
adaptive PSO [96]				
beam-ACO [95]				
MCS method [98]				
HHO method [99]				
GWO approach [100]				
Whale Optimization [101]				
Chimp Optimization [102]				
Neural Network based Segmentation [103]				
SUFEMO (Proposed)				

Fig. 8. Comparison of various techniques using I_{001} for various count of the clusters.

Table 4
Brief details of some images.

Id	Image view	Image source	Description	Courtesy
I_{001}	Saggital	[81]	This is a CT image of the chest area of 64 years of age, female patient who is contaminated with COVID-19 from Wenzhou, China. Some significant perceptions are accounted for, for example, ground-glass opacities in the right upper, center, and lower lobes and furthermore in the lingula. Some atelectasis can be seen in the right lower lobe.	Omir Antunes Paiva, Dr. Rodrigo Caruso Chate, Wenzhou Medical University, and coronacases.org
I_{002}	Coronal	[82]	This is a CT examined the image of the chest area of 55 years of age, female patient who is contaminated with COVID-19 from Wenzhou, China. Some significant perceptions are accounted for, for example, different ground-glass opacities with reticulation and little foci of solidification in every single aspiratory lobe.	
I_{003}	Axial	[83]	This is a CT image of the chest area of 55 years of age, female patient who is contaminated with COVID-19 from Taoyuan General Hospital, Taoyuan, Taiwan. Some significant perceptions are accounted for, for example, numerous ground-glass opacities with reticulation and little foci of consolidation in every pneumonic lobe.	NA
I_{004}	Coronal	[84]	This is a CT examination image of the chest locale of 70 years of age, male patient who is tainted with COVID-19 from Riccione, Italy. Some significant perceptions and elements are accounted for, for example, ground-glass opacities in the lower right and the upper lobes and Paraseptal emphysema in the upper lobes.	Dr. Domenico Nicoletti, Radiopaedia.org, rID: 74724
I_{005}	Axial	[85]	This is a CT image of the chest area of 70 years of age, female patient who is contaminated with COVID-19 from Ospedale Santo Spirito. Rome, Italy. Some significant perceptions and elements are accounted for, for example, respective ground-glass opacities and mediastinal lymph hubs.	Dr. Fabio Macori, Radiopaedia.org, rID: 74887
I_{006}	Axial	[86]	This is a CT image of the chest area of a 54 years of age, male patient who is contaminated with COVID-19 from Myongji Hospital, Goyang, Korea. Some significant perceptions and components are accounted for, for example, combination in the right upper lobes and ground-glass opacities in both lower lobes.	
I_{007}	Coronal	[87]	This is a CT scan of the chest locale of a 50 years of age, male patient who is tainted with COVID-19 from Italy.	NA
I_{008}	Axial	[88]	This is a CT image of the chest district of a 45 years of age, male patient who is contaminated with COVID-19 from Italy. Some significant perceptions and provisions are accounted for like various ground glass thickness.	
I_{009}	Axial	[89]	This is a CT image of the chest area of 50 years of age, male patient who is tainted with COVID-19 from Iran. Some significant perceptions and provisions are accounted for, for example, two-sided ground-glass opacities in the two lungs.	Dr. Bahman Rasuli, Radiopaedia.org, rID: 74576
I_{010}	Frontal	[90]	This picture is gathered from 25 years of age, male patient.	Dr. Andrew Dixon, Radiopaedia.org, rID: 36676

proposed approach performs well by and large and can be deployed in real-life scenarios. The robustness and convergence are likewise introduced in sub-segments 4.4. also, 4.5. individually. Fig. 8 illustrates the segmentation outcome that are obtained using the proposed SUFEMO approach.

From the detailed quantitative analysis, one important point can be noticed that the obtained values of the clustering indices sometimes fluctuating with the increasing number of clusters i.e., sometimes the value of the cluster validity indices increases and sometimes decreases. Actually, the value of the cluster validity indices depends on several factors. For example, the value of the Davies–Bouldin index depends on the two major deciding factors: the intra-cluster and the inter-cluster distances (please refer to Eq. (21)). When the count of the clusters increases then, the formation of the clusters may influence the values of the validity indices. It can also be noted that the underlying dataset may also influence the values of the cluster validity indices. Moreover, the result of the metaheuristic optimization procedure does

not guarantee the same results every time [7,104,105]. Hence, the value of the cluster validity indices may vary with increasing and/or decreasing number of clusters.

4.4. Analysis of the robustness

In this subsection, the robustness of the proposed approach is represented against various sorts of noise. Moreover, the compactness of the superpixels is also illustrated.

4.4.1. Robustness against noise
Biomedical images are always susceptible to noise. The robustness of the underlying segmentation scheme is an extremely essential point from the perspective of the biomedical image segmentation that is to be evaluated before deploying the model in real-life scenarios. In this subsection, the actual image I_{008} is intentionally corrupted with different types of noise and then

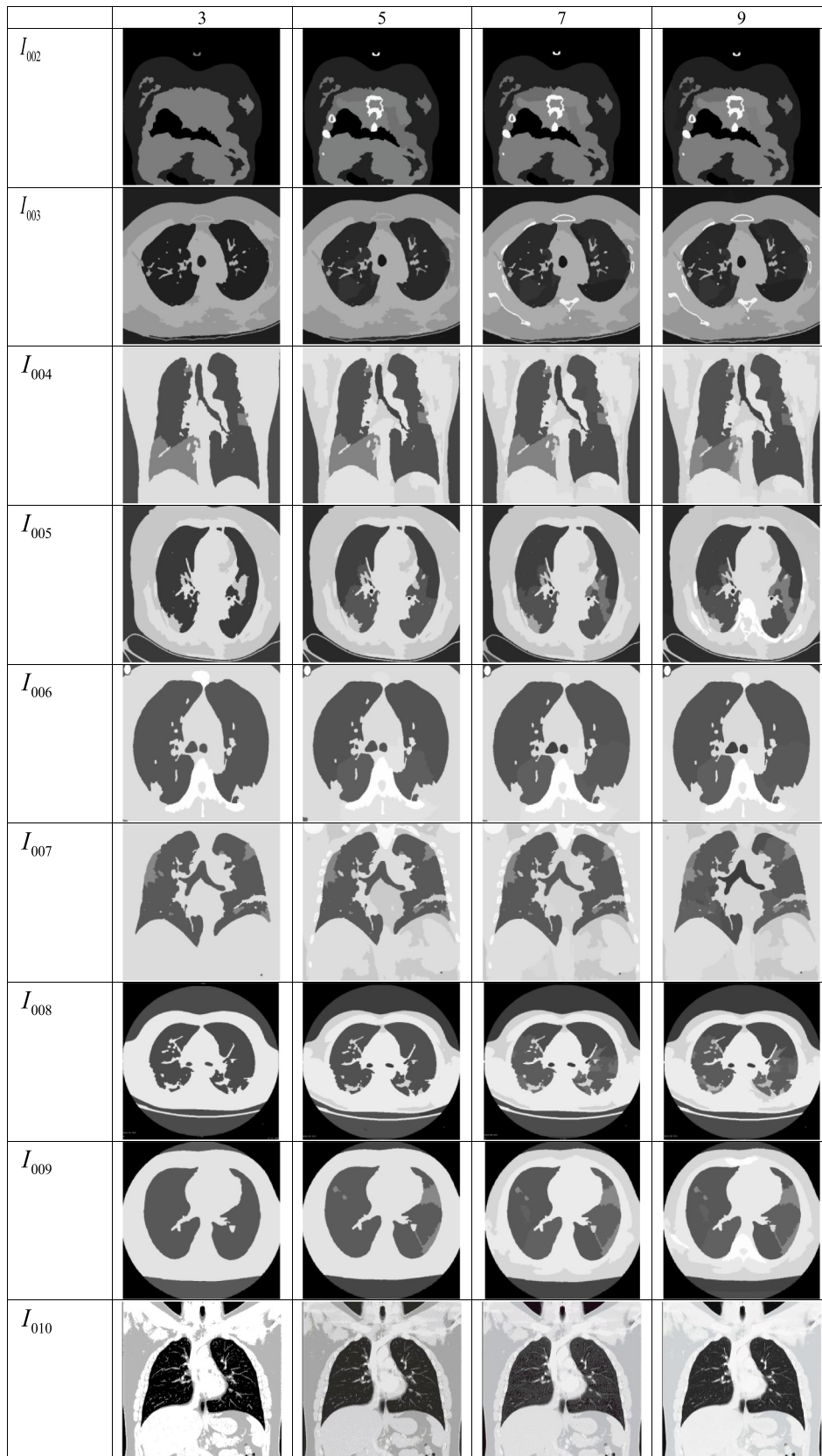|	3	5	7	9
I_{002}				
I_{003}				
I_{004}				
I_{005}				
I_{006}				
I_{007}				
I_{008}				
I_{009}				
I_{010}				

Fig. 9. Segmented results for various number of clusters which are acquired by applying the SUFEMO technique.

Table 5

The quantitative examination of various segmentation strategies utilizing the (The satisfactory values are featured in strong face).

Index	Image	Applied algorithm	Count of the clusters			
			3	5	7	9
Davies–Bouldin	Average (310 images)	Efficient GA [97]	2.057389792	2.341342543	2.631067668	2.182999317
		Adaptive PSO [96]	1.466742939	2.262712553	2.300312783	1.649374921
		Beam-ACO [95]	1.49016067	1.906178838	2.109355593	1.852796881
		MCS method [98]	2.125579881	2.355334741	1.756786889	1.832064307
		HHO method [99]	1.615224562	1.702627053	2.204451965	2.647738311
		GWO approach [100]	1.835247126	1.767716428	2.946051439	2.722753129
		Whale optimization [101]	1.767607021	2.528863859	2.803699012	2.316640263
		Chimp optimization [102]	2.415340941	2.350907067	2.433318413	2.553789173
		Neural network based segmentation [103]	1.606792734	**1.693970454**	**1.542606235**	2.297489919
		SUFEMO (Proposed)	**1.421301735**	1.812008792	1.687189337	**1.502481616**
Xie–Beni Index	Average (310 images)	Efficient GA [97]	1.624786762	1.709276519	2.207538007	2.649905004
		adaptive PSO [96]	1.849336068	1.786084272	2.948651807	2.735604899
		Beam-ACO [95]	1.784413031	2.534017353	2.806131272	2.335561186
		MCS method [98]	2.435244805	2.353755926	2.446036152	2.554270162
		HHO method [99]	2.038041	2.334152	2.612432	2.9165278
		GWO approach [100]	1.448495	2.246186	2.295493	2.631099
		Whale optimization [101]	1.475947	1.904366	2.105878	2.833088
		Chimp optimization [102]	2.107597	2.351055	2.754129	2.819813
		Neural network based segmentation [103]	1.61375	**1.683281**	**2.044525**	2.595974
		SUFEMO (Proposed)	**1.628119075**	1.697662119	**2.246409944**	**2.310486157**
Dunn index	Average (310 images)	efficient GA [97]	1.326722693	2.295283281	2.334360301	2.013982282
		Adaptive PSO [96]	1.517242172	1.803836769	1.405798931	1.331685373
		Beam-ACO [95]	1.458856701	1.438020506	2.154291777	2.655296748
		MCS method [98]	1.906901194	1.853224645	**2.831798973**	3.028592536
		HHO method [99]	1.230797	1.306074	2.353937	2.016582
		GWO approach [100]	1.726747	1.815292	1.9218	2.244343
		Whale optimization [101]	1.459989	1.552861	2.455488	2.763597
		Chimp optimization [102]	2.122828	1.66564	2.44328	2.732422
		Neural network based segmentation [103]	2.546459	2.504361	2.362737	2.28769
		SUFEMO (Proposed)	**2.584698504**	**2.588595748**	2.350004016	**2.868974087**
β index	Average (300 images)	Efficient GA [97]	0.48298906	1.855825929	1.935245603	1.513778012
		Adaptive PSO [96]	2.199301495	2.028453938	2.538635827	2.158815625
		Beam-ACO [95]	1.442986088	2.053681742	1.724977482	1.834309177
		MCS method [98]	2.749255434	2.711009201	**3.993628751**	2.967283554
		HHO method [99]	2.486583	2.864695	2.941107	1.92769
		GWO approach [100]	2.517785	2.947065	2.855919	2.859128
		Whale optimization [101]	**2.954762**	2.367244	2.728644	2.449435
		Chimp optimization [102]	2.766324	2.521449	3.011658	2.969639
		Neural network based segmentation [103]	2.849432	**3.157295**	3.77819	2.936146
		SUFEMO (Proposed)	2.830809221	3.142069236	3.790172244	**2.993016698**

processed with the proposed approach. The outcomes are presented in Fig. 10.

From Fig. 10, it can be observed that the noisy images do not have a significant impact either on the superpixel computation or the final segmented outcome. The gradient information helps to overcome the noise susceptibility of this approach.

4.4.2. Compactness of the superpixels

The compactness of the superpixels is an important parameter that is required to be analyzed to test the robustness of the system. The compactness of the superpixels can be measured by checking the boundaries of the superpixels. A superpixel with a smooth boundary is considered a compact superpixel. The isoperimetric quotient is used to mathematically express the compactness of the superpixel [106]. For the ith superpixel S_i, the isoperimetric quotient can be mathematically computed using Eq. (25).

$$IQ_{S_i} = \frac{4 \cdot \pi \cdot AREA(S_i)}{PERI(S_i) \cdot PERI(S_i)} \tag{25}$$

In this equation, $AREA(S_i)$, and $PERI(S_i)$ denotes the area and the shape perimeter of the ith superpixel S_i. The compactness C_s of a superpixel image can be computed using Eq. (26). Eq. (26) is based on the isoperimetric quotient IQ_{S_i} that ranges over the set of the superpixels Θ that is obtained by segmenting the image

IMG.

$$C_\Theta = \sum_{S_i \in \Theta} IQ_{S_i} = \frac{|S_i|}{|IMG|} \tag{26}$$

In this equation, $|S_i|$ denotes the size of the ith superpixel that is used to normalize the sum of the isoperimetric quotient IQ_{S_i} over the set of the superpixels Θ.

Experiments are carried out on I_{008} by adding two-dimensional Gaussian blur. Fig. 11 illustrates the obtained results. This figure depicts an increase in the compactness value concerning the Gaussian Sigma values. The object boundaries are affected by the higher values of the sigma. Hence, the obtained superpixels clung well to the limits and keep an unpredictable shape.

4.5. Investigation of the convergence rate

The rate of convergence examination is a significant subject of conversation which comprehends the performance of the proposed Algorithm just as some other standard strategies. In this subsection, the convergence of the proposed strategy is investigated graphically for various clusters utilizing the image I_{001} and the graphical comparison can be observed in Fig. 12. he values of the Xie–Beni index are considered to play out a near investigation of the convergence. The proposed technique beats some other standard strategies as far as the segmentation quality as well as, additionally as far as convergence and it tends to be effectively perceived from Fig. 12.

	Noisy Image	Gradient Information	Superpixel	Segmented outcome
(A)				
(B)				
(C)				
(D)				
(E)				

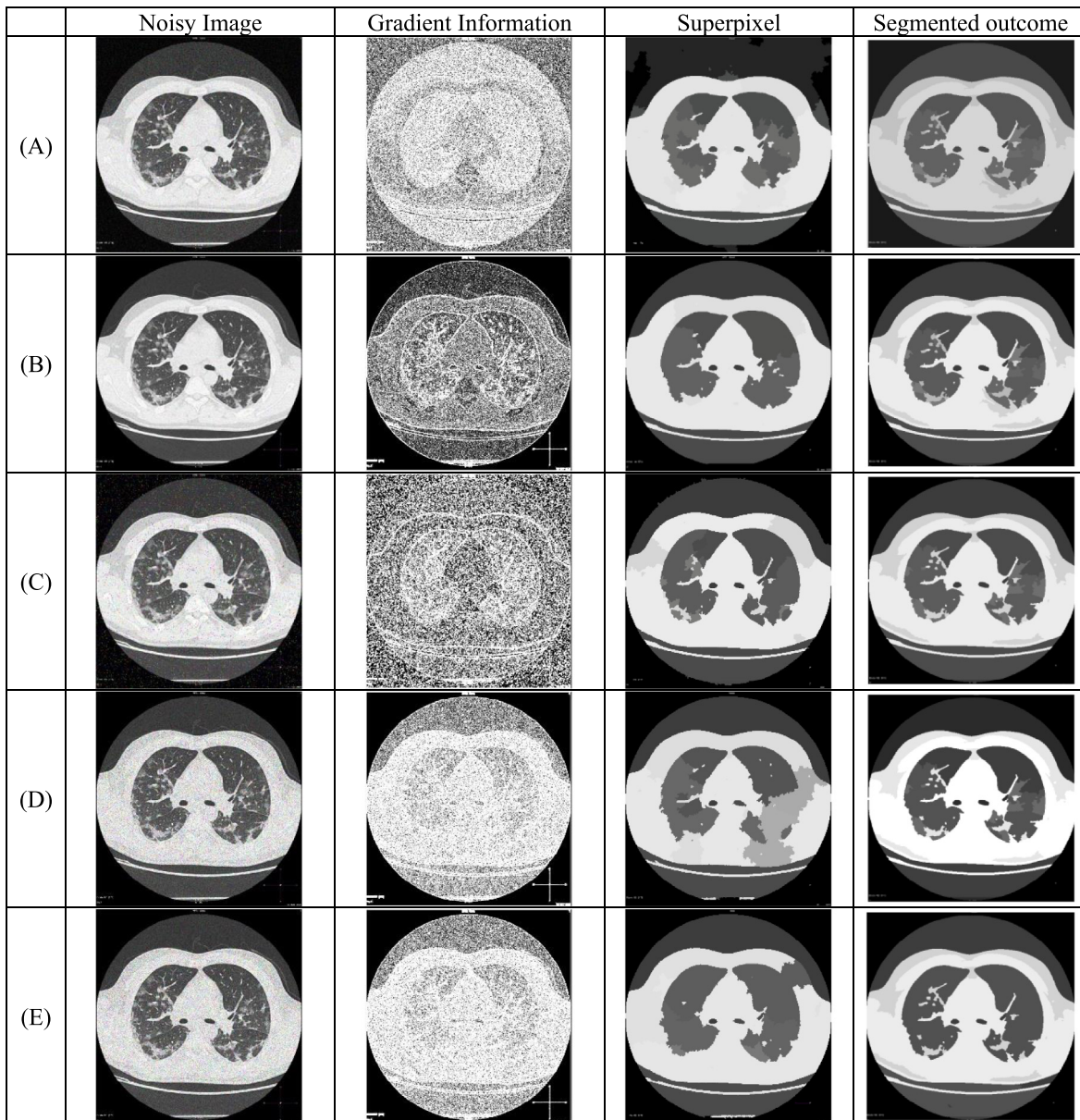**Fig. 10.** Graphical analysis of the impact of noise on the segmentation approach. The experiment is carried out by intentionally corrupting the actual image with (A) Gaussian noise, (B) Poisson noise, (C) Salt & Pepper noise, (d) Speckle noise, and (e) Random noise.
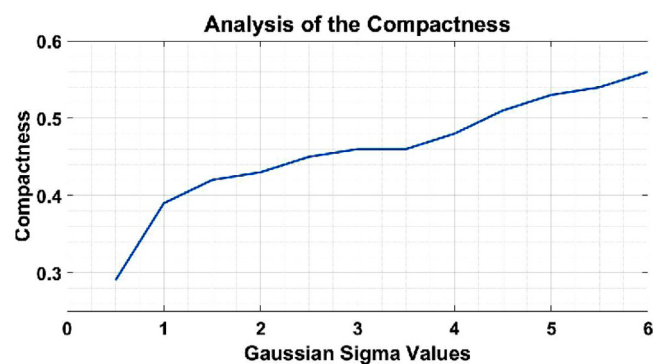

Fig. 11. Analysis of the compactness. In the *x*-axis, the Gaussian sigma values are plotted and, in the *y*-axis, the value of the compactness is plotted.
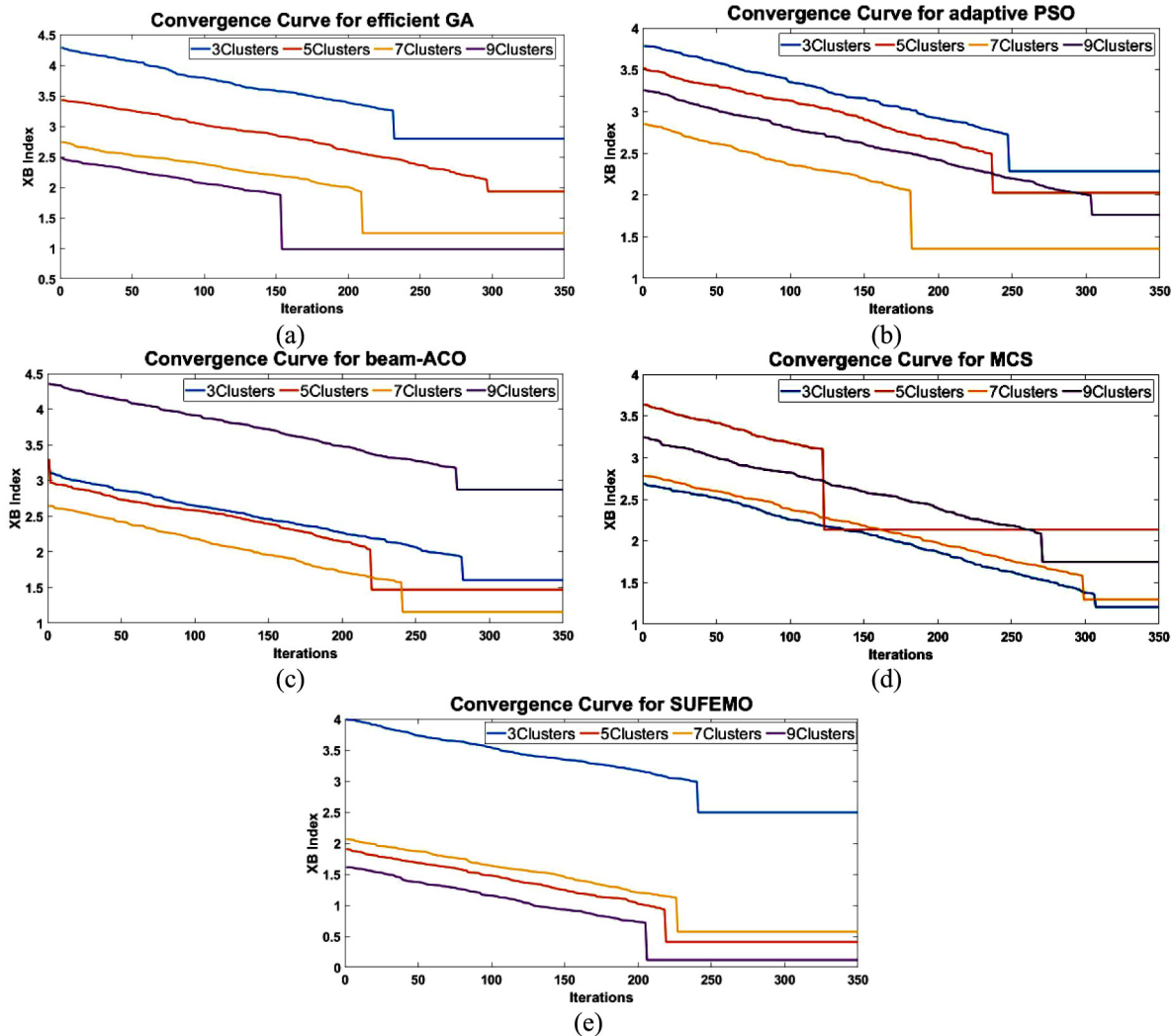
Fig. 12. The graphical investigation of the convergence for various strategies and for various numbers of clusters. The value of the Xie–Beni file for the image I_{001} is plotted in the Y-axis and the number of iterations is plotted in the X-axis in the curves which are plotted using (a) efficient genetic algorithm, (b) adaptive PSO, (c) Beam-ACO, (d) MCS, (e) SUFEMO (proposed).

4.6. Investigation of the running time

Running time is one of the important metrics to be discussed. In Table 6, the running times that are obtained using five different approaches are reported. All four clustering indices are considered and for each index, four different clusters are taken into account.

The proposed approach takes advantage of the upsides of the superpixel that can be utilized to lessen the computational overhead by diminishing a lot of spatial data. Besides, the customary fuzzy objective work is changed appropriately to take on the upsides of the superpixel. From the detailed investigation and various tests, it tends to be reasoned that the proposed approach performs well and can be deployed in real-life scenarios.

5. Discussion

This work uses the EMO approach as the underlying optimization procedure. EMO approach is a recently developed metaheuristic procedure and being applied to solve different optimization problems [107]. However, in this application scenario, other optimization approaches can also be adopted. However, the proposed approach is compared with some standard metaheuristic approaches-based multilevel thresholding approaches and it can

be observed that the proposed approach outperforms the others in most of the scenarios. This work adopts the soft computing approach to segment the biomedical images because the regions in the biomedical images typically does not have crisp boundaries. Hence, it is difficult to identify the boundaries to extract different regions of the biomedical images. The inherent fuzzy nature of the biomedical images compelled us to think about soft computing tools. It is beneficial to use fuzzy and other soft computing-based tools to generate effective and realistic segmented outcome.

As discussed earlier, the type-2 fuzzy clustering approach is used in this work The type-1 fuzzy frameworks experience the ill effects of commotion and relative participation esteems which is unsafe to the fragmented result. This issue can be settled by applying the type-2 fuzzy framework where the uncertainty of a point is high if the membership value is low as well as the other way around [61–63]. In addition, the participation esteems are considered as weights. The significant benefits of type-2 fuzzy framework based clustering approach are referenced beneath [64]:

d. Uncertainties can be efficiently modeled and a point with lesser uncertainty has a higher impact than a point with higher uncertainty.

Table 6
Highlight of the average running time (in seconds). (Here, bold values represent the optimum values).

Validity index	No. of clusters	Efficient GA [97]	Adaptive PSO [96]	Beam-ACO [95]	MCS method [98]	SUFEMO (Proposed)
Davies–Bouldin	3	**4.238418286**	5.632118308	6.06447709	6.307048099	4.77056936
	5	**5.444965604**	7.75891844	7.307822803	6.447645005	7.66689135
	7	**7.879990563**	10.12569268	8.691811737	9.725285724	9.129117881
	9	10.68855921	11.96574569	12.6046745	11.30800471	**10.01429496**
Xie–Beni	3	**4.850831941**	7.995793286	7.567331723	6.929007742	7.259451485
	5	7.932629598	**5.916318599**	9.483773293	7.722648938	9.639173777
	7	9.890749976	**8.449789724**	10.58437821	10.58981477	10.75583124
	9	15.05453316	**11.16081822**	11.91401094	13.93447588	12.32138991
Dunn	3	**4.690458291**	5.155860842	6.147312867	6.790409689	6.939818022
	5	**5.408766931**	5.767406518	6.222150591	6.776808716	8.155608882
	7	**12.01642909**	12.89436908	12.15626026	12.45983762	8.88412483
	9	16.04382736	14.56314442	13.52474775	15.12863995	**11.94132605**
β	3	5.792550727	6.151831356	**5.624232866**	5.824847612	7.470809597
	5	8.528548345	9.155279873	7.578897528	**7.137288349**	7.4540355
	7	13.66627615	15.54143115	16.47834472	**10.10033398**	12.23066683
	9	14.76384207	15.55533245	15.09298717	13.23624317	**12.84600408**

e. In the viable situation, some more sensible yields can be created by the type-2 fuzzy clustering framework contrasted with the type-1 fuzzy clustering frameworks.

f. Higher noise invulnerability can be accomplished.

Hence, it can be observed that selection of the soft computing tools and type-2 fuzzy clustering approach helps to obtain better results and to produce realistic clustering outcome. The proposed approach is used to segment 300 CT scan images that are randomly selected which are obtained from different countries of the world [79,80]. The proposed approach can be applied for different chest CT scans i.e., various other data sources can also be used. Moreover, it will be interesting to apply the proposed approach on various other types of images. Here, four standard cluster validation approaches are selected to quantify the obtained outcomes. These four cluster validation approaches are massively used in quantitative analysis of various clustering outcomes. These approaches do not directly affect the segmentation outcome but helps to find out the performance of a certain approach. Apart from these approaches, some other approaches can also be used to test the cluster validity. It can be an interesting future work.

The proposed approach is basically an unguided clustering approach where the fuzzy EMO approach is used to determine the optimal cluster centers from the set of superpixels. Hence, there are no steps involved that detects or extracts features from the images. Again, the proposed approach is a simple and novel technique to highlight different section of an image through segmentation. This approach is not a classification approach i.e., it cannot automatically detect unhealthy regions of a lung but, instead of that, it can perform the segmentation and can precisely highlight various segments that can help physicians and other domain experts to effectively analyze these images so that they can take quick decision about the patient. The incorporation of the novel superpixel computation approach reduces the overhead of processing significantly large amount of spatial information.

6. Conclusion

This article proposes an efficient structure for the radiological image segmentation dependent on superpixel and fuzzy metaheuristics and the proposed technique can be profoundly useful in the screening system of COVID-19 by deciphering the chest CT pictures naturally. The proposed SUFEMO strategy is tried on various CT scan pictures of the chest area which are gathered from the COVID-19 tainted patients from various areas of the world. As talked about before, a threefold contribution can be seen in this work. Above all else, the enormous measure of spatial

data can be proficiently taken care of by the proposed superpixel-based methodology. The proposed fuzzy EMO approach is useful in effectively deciding the cluster centers which is the second significant contribution. The type-2 fuzzy target work is refreshed as needs be to take advantage of the upsides of the super-pixel, which is the third significant commitment. This original methodology can be useful in the early screening of associated patients to battle the spread with the COVID-19 infection. From the point-by-point investigation of the proposed approach, it may be presumed that the proposed approach can proficiently and viably play out the work of segmentation of the chest CT scans. From both, visual and quantitative exploratory outcomes, it tends to be effortlessly surmised that the proposed SUFEMO strategy outflanks a portion of the standard methodologies. The utilization of the superpixel approach lessens the computational overhead that is related to the handling of a high measure of spatial data. It likewise assists with working on the pace of combination of the proposed strategy contrasted with different methodologies. Subsequently, the proposed approach can be adapted to help doctors by creating precise segmented outcomes. Additionally, the proposed approach can save some time in light of the fact that no sample assortment is required. As talked about before, the proposed work can be exceptionally valuable to disconnect the speculated patients so that, the local area spread of this sickness can be halted and it is a significant contribution of the proposed work from the clinical perspective. The RT-PCR test is tedious (the turnaround time is roughly 10–15 h in the wake of getting the example from the presumed patient), and the outcome might be gotten following a few days if the waiting queue is long. Detailed experiments utilizing radiological pictures can essentially build the shot at early discovery of this exceptionally irresistible illness. Once more, the proposed work cannot be utilized as a substitute for the RT-PCR test, be that as it may, it is a less complex and quicker method of early screening. Some noticeable features have been seen in the chest CT pictures of the COVID-19 contaminated patients (which are represented in Table 1) which are useful in the screening system. With the utilization of the proposed technique, the screening system can be sped up advantageously. One major limitation of the proposed work is that the cluster count should be supplied externally i.e., the proposed approach cannot determine the cluster count from the underlying dataset.

6.1. Major contributions

A threefold contribution can be observed in this work. First of all, the huge spatial information can be productively handled by the proposed superpixel-based approach. A single value is used by the proposed work to represent a set of pixels that reduces the
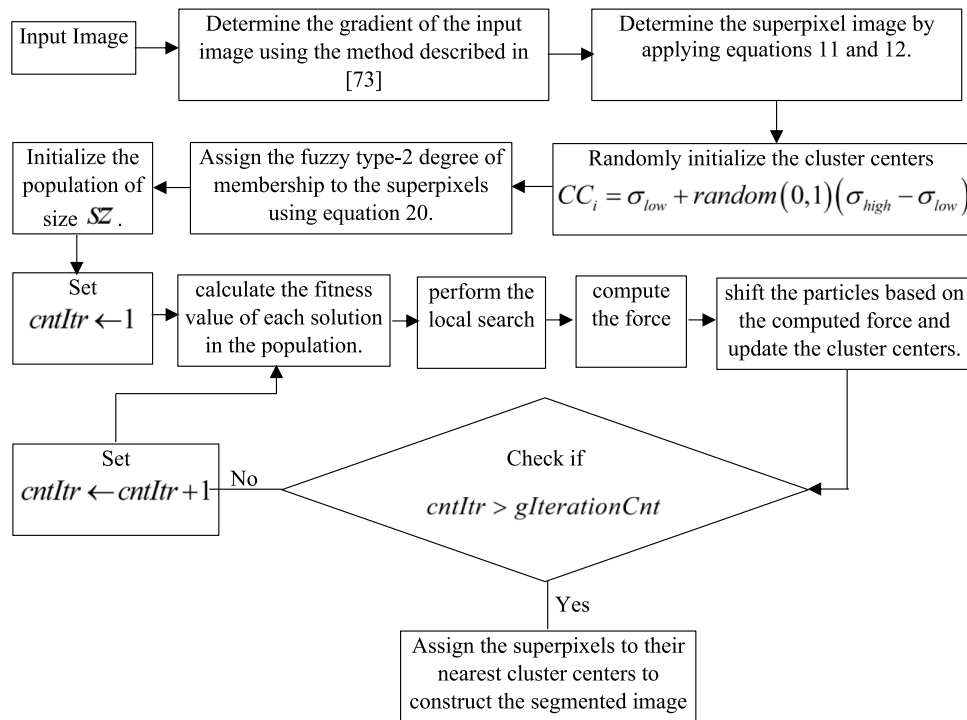
Fig. A.1. Detailed schematic flow diagram of the proposed approach.

processing overhead. The application of the EMO method coupled with type-2 fuzzy extension is another important contribution of this work. The proposed fuzzy EMO approach is helpful in efficiently determining the cluster centers which is the second major contribution. The proposed objective function is updated accordingly to effectively utilize the benefits of the superpixel, and it is the third important contribution. This novel approach can be helpful in determining the suspects to fight against the spread of the COVID-19 virus. Hence, the following are the key advantages of this approach:

1. Efficient handling of huge spatial information is possible.
2. Cluster centers can be automatically determined without depending on the choice of initial cluster centers.
3. The fuzzy objective function is modified to exploit the advantages of superpixels.
4. There is no need to use any manual delineations for segmentation purposes.

6.2. Practical implications

The proposed work is extremely beneficial to create a barrier between the suspected patients and the healthy patients so that, the drastic spread of this disease can be stopped and it is a major clinical significance of the proposed work. The gold standard test RT-PCR consumes a considerably large time (the required turnaround time for the RT-PCR test is nearly 10–15 h after the sample is collected), and patients may have to wait for more than three days if the queue is long. Investigation using radiological images can significantly increase the chance of early detection of this highly infectious disease. The proposed SUFEMO method will be certainly helpful for automated computer-based diagnostics procedures to accelerate the diagnostic process. Also, the proposed unsupervised segmentation technique is applied to different radiological images with different views, to demonstrate the strength and the practical utility. A significantly large volume of spatial information can be efficiently taken care of and it makes

the proposed method useful to process the CT scan stacks. It can be helpful to assess the condition of a patient in a more detailed way.

6.3. Limitations of the proposed approach

The proposed approach is efficient enough however, this approach cannot determine the number of clusters automatically and that is one of the major limitations of this approach. Although the superpixel approach is capable enough in handling noise, the segmentation approach does not take the noise into account, if present. This approach is not a classification approach i.e., it cannot automatically detect unhealthy regions of a lung but, instead of that, it can perform the segmentation and can precisely highlight various segments that can help physicians and other domain experts to effectively analyze these images so that they can take quick decision about the patient. So, absence classification mechanism can be incorporated later on. Automatic tuning of the hyperparameters is also not available in this approach.

6.4. Future scopes

In some future works, at first, the number of clusters can be determined automatically. The automatic estimation of the count of the clusters can make this approach more robust and effective for real-life applications. Secondly, the proposed approach can be applied to different types of images including other modalities. Thirdly, the proposed work can be further enhanced by improving the noise handling capability. Although the superpixel approach is capable enough in handling noise, the segmentation approach does not take the noise into account, if present. Apart from these works, it will be interesting to incorporate an approach that can automatically get the optimized values for the controlling parameters of the EMO approach (i.e., automatic tuning of the controlling parameters) that are given in Table 3. In this work, these parameters are tuned manually but, manual tuning may not be practically feasible for different types of images. Hence, automated tuning approaches can be beneficial in obtaining better segmentation performance and also achieve better performance.

Table A.1

Summary of the symbols used in this work.

Symbol	Description	Remarks
$\vec{F}_{ij}$	Represents the force that is exerted by a particle in EMO approach	
p_i	A particle in the EMO approach	
$f(q)$	Represents a non-linear function	$f : \mathbb{R}^n \to \mathbb{R}$, Please refer Eq. (1)
Q	Represents a region which is bounded by the lower and the upper bounds low_j and $high_j$ respectively	$Q = \left\{ \begin{array}{l} q \in \mathbb{R}^n \| \\ low_j \leq q_j \leq high_j, j = 1, 2, 3, \ldots \ldots, n \end{array} \right\}$ Please refer Eq. (1)
sz	The size of the initial population	
$gIterationCnt$	Global iteration counter	Please refer Algorithm 1
$lIterationCnt$	Local iteration counter	Please refer Algorithm 1
τ	The controlling parameter of the local search	$\tau \in [0, 1]$
μ_{ij}^{ϕ}	Represents the membership value of the point x_i to the jth cluster.	$\sum_{j=1}^{nCen} \mu_{ij} = 1 \, for \, i = 1, 2, 3, \ldots \ldots, nPnt$ Please refer Eq. (2)
ϕ	Represents the fuzzifier	Please refer Eq. (2)
Obj_{ϕ}	The fuzzy objective function	Please refer Eq. (2)
$nPnt$	Represents the number of available data points and the number of cluster centers.	Please refer Eq. (2)
$nCen$	Represents the number of available data points and the number of cluster centers.	Please refer Eq. (2)
c_j	The jth cluster center.	Please refer Eq. (4)
ω_{ij}	The modified membership value in type-2 fuzzy clustering system	Please refer Eq. (5)
κ	A small threshold value	Please refer Algorithm 2
ψ	Morphological erosion operation	Please refer Eq. (9)
ζ	Morphological dilation operation	Please refer Eq. (10)
Ω^{ψ}	Morphological erosion-based reconstruction operation	Please refer Eq. (7)
Ω^{ζ}	Morphological dilation-based reconstruction operation.	Please refer Eq. (8)
I	The original image	Please refer Eq. (13)
$\tilde{I}$	The marker image	Please refer Eq. (14)
υ	The structuring Element	Please refer Eqs. (13), and (14)
o	The morphological opening operation	Please refer Eq. (11)
ς	The morphological closing operation	Please refer Eq. (12)
χ	The controlling parameter for the structuring elements.	The count of the structuring elements can be controlled depending on the range of the controlling parameter $\left[\chi_{low}, \chi_{high} \right]$ where χ_{low} and χ_{high} denotes the lower and the upper bounds of the controlling parameter χ.
ε	A small threshold value that can be used as the error rate and depending on this value the local minima from the gradient images can be discarded.	Please refer Eq. (16)
σ_{low} and σ_{high}	Represents the minimum and the maximum values of the representative point of a superpixel.	Please refer Algorithm 3
$DBIndex$	Represents the Davies–Bouldin index	Please refer Eq. (21)
$XBIndex$	Represents the Xie–Beni index	Please refer Eq. (22)
DI_n	Represents the Dunn index	Please refer Eq. (23)
β	Represents the β index	Please refer Eq. (24)
IQ_{S_i}	The isoperimetric quotient for the ith superpixel S_i	Please refer Eq. (25)
$AREA(S_i)$	Area of the ith superpixel S_i.	Please refer Eq. (25)
$PERI(S_i)$	The shape perimeter of the ith superpixel S_i.	Please refer Eq. (25)
C_s	Compactness of a superpixel image	Please refer Eq. (26)
Θ	Set of superpixel	Please refer Eq. (26)

CRediT authorship contribution statement

Shouvik Chakraborty: Solution formulation, Conceptualization, Methodology, Software development, Article writing, Investigation. **Kalyani Mali:** Formal analysis, Resources, Review, Editing, Supervision.

Declaration of competing interest

The authors declare that they have no known competing financial interests or personal relationships that could have appeared to influence the work reported in this paper.

Data availability

Citations added

Appendix A

See Fig. A.1.

Appendix B

See Table A.1.

References

[1] T.M. Mitchell, Mach. Learn. (1997) http://dx.doi.org/10.1145/242224.242229.

[2] S. Chakraborty, K. Mali, Applications of advanced machine intelligence in computer vision and object recognition : emerging research and opportunities, n.d.

[3] S. Chakraborty, S. Chatterjee, A.S. Ashour, K. Mali, N. Dey, Intelligent computing in medical imaging: A study, in: N. Dey (Ed.), Adv. Appl. Metaheuristic Comput., IGI Global, 2017, pp. 143–163, http://dx.doi.org/10.4018/978-1-5225-4151-6.ch006.

[4] A.L. Samuel, Some studies in machine learning using the game of checkers, IBM J. Res. Dev. 44 (2000) 207–219, http://dx.doi.org/10.1147/rd.441.0206.

[5] S. Chakraborty, K. Mali, An overview of biomedical image analysis from the deep learning perspective, in: S. Chakraborty, K. Mali (Eds.), Appl. Adv. Mach. Intell. Comput. Vis. Object Recognit. Emerg. Res. Oppor., IGI Global, 2020, http://dx.doi.org/10.4018/978-1-7998-2736-8.ch008.

[6] S. Chakraborty, K. Mali, Application of multiobjective optimization techniques in biomedical image segmentation—A study, in: Multi-Objective Optim., Springer Singapore, Singapore, 2018, pp. 181–194, http://dx.doi.org/10.1007/978-981-13-1471-1_8.

[7] S. Chakraborty, K. Mali, A. Banerjee, M. Bhattacharjee, A Biomedical Image Segmentation Approach using Fractional Order Darwinian Particle Swarm Optimization and Thresholding, Springer, 2021, pp. 299–306, http://dx.doi.org/10.1007/978-981-15-9433-5_29.

[8] A. Fourcade, R.H. Khonsari, Deep learning in medical image analysis: A third eye for doctors, J. Stomatol. Oral Maxillofac. Surg. 120 (2019) 279–288, http://dx.doi.org/10.1016/j.jormas.2019.06.002.

[9] S. Chakraborty, K. Mali, K. Ghosh, A. Sarkar, Penalized fuzzy C-means coupled level set based biomedical image segmentation, in: Lect. Notes Networks Syst., Springer Science and Business Media Deutschland GmbH, 2021, pp. 279–287, http://dx.doi.org/10.1007/978-981-15-9433-5_27.

[10] C.L. Sistrom, P.A. Dang, J.B. Weilburg, K.J. Dreyer, D.I. Rosenthal, J.H. Thrall, Effect of computerized order entry with integrated decision support on the growth of outpatient procedure volumes: Seven-year time series analysis, Radiology 251 (2009) 147–155, http://dx.doi.org/10.1148/radiol.2511081174.

[11] C.E. Kahn, C.P. Langlotz, E.S. Burnside, J.A. Carrino, D.S. Channin, D.M. Hovsepian, D.L. Rubin, Toward best practices in radiology reporting, Radiology 252 (2009) 852–856, http://dx.doi.org/10.1148/radiol.2523081992.

[12] S. Chakraborty, M. Roy, S. Chatterjee, K. Mali, S. Banerjee, Detection of HIV-1 progression phases from transcriptional profiles in ex vivo CD4+ and CD8+ T cells using meta-heuristic supported artificial neural network, Multimedia Tools Appl. 81 (2022) 15103–15126, http://dx.doi.org/10.1007/S11042-022-12534-7, 8111.

[13] P. Lakhani, A.B. Prater, R.K. Hutson, K.P. Andriole, K.J. Dreyer, J. Morey, L.M. Prevedello, T.J. Clark, J.R. Geis, J.N. Itri, C.M. Hawkins, Machine learning in radiology: Applications beyond image interpretation, J. Am. Coll. Radiol. 15 (2018) 350–359, http://dx.doi.org/10.1016/j.jacr.2017.09.044.

[14] S. Hore, S. Chakraborty, S. Chatterjee, N. Dey, A.S. Ashour, L. Van Chung, G. Nguyen, D.-. Nhuong Le, An integrated interactive technique for image segmentation using stack based seeded region growing and thresholding, Int. J. Electr. Comput. Eng. 6 (2016) 2773–2780, http://dx.doi.org/10.11591/ijece.v6i6.11801.

[15] WHO coronavirus (COVID-19) dashboard | WHO coronavirus (COVID-19) dashboard with vaccination data, 2021, https://covid19.who.int/ (accessed May 28, 2021).

[16] J.P. Kanne, B.P. Little, J.H. Chung, B.M. Elicker, L.H. Ketai, Essentials for radiologists on COVID-19: An update-radiology scientific expert panel, Radiology (2020) 200527, http://dx.doi.org/10.1148/radiol.2020200527.

[17] Z.Y. Zu, M. Di Jiang, P.P. Xu, W. Chen, Q.Q. Ni, G.M. Lu, L.J. Zhang, Coronavirus disease 2019 (COVID-19): A perspective from China, Radiology (2020) 200490, http://dx.doi.org/10.1148/radiol.2020200490.

[18] A. Bernheim, X. Mei, M. Huang, Y. Yang, Z.A. Fayad, N. Zhang, K. Diao, B. Lin, X. Zhu, K. Li, S. Li, H. Shan, A. Jacobi, M. Chung, Chest CT findings in coronavirus disease-19 (COVID-19): Relationship to duration of infection, Radiology (2020) 200463, http://dx.doi.org/10.1148/radiol.2020200463.

[19] T. Ai, Z. Yang, H. Hou, C. Zhan, C. Chen, W. Lv, Q. Tao, Z. Sun, L. Xia, Correlation of chest CT and RT-PCR testing in coronavirus disease 2019 (COVID-19) in China: A report of 1014 cases, Radiology (2020) 200642, http://dx.doi.org/10.1148/radiol.2020200642.

[20] Y. Fang, H. Zhang, J. Xie, M. Lin, L. Ying, P. Pang, W. Ji, Sensitivity of chest CT for COVID-19: Comparison to RT-PCR, Radiology (2020) 200432, http://dx.doi.org/10.1148/radiol.2020200432.

[21] P. Torkian, N. Ramezani, P. Kiani, M.R. Bax, S. Akhlaghpoor, Common CT findings of novel coronavirus disease 2019 (COVID-19): A case series, Cureus 12 (2020) http://dx.doi.org/10.7759/cureus.7434.

[22] S. Chakraborty, K. Mali, SUFMACS: a machine learning-based robust image segmentation framework for covid-19 radiological image interpretation, Expert Syst. Appl. (2021) 115069, http://dx.doi.org/10.1016/j.eswa.2021.115069.

[23] D. Caruso, M. Zerunian, M. Polici, F. Pucciarelli, T. Polidori, C. Rucci, G. Guido, B. Bracci, C. de Dominicis, A. Laghi, Chest CT features of COVID-19 in Rome, Italy, Radiology (2020) 201237, http://dx.doi.org/10.1148/radiol.2020201237.

[24] S. Chakraborty, K. Mali, Biomedical image segmentation using fuzzy multilevel soft thresholding system coupled modified cuckoo search, Biomed. Signal Process. Control 72 (2022) 103324, http://dx.doi.org/10.1016/J.BSPC.2021.103324.

[25] S. Chakraborty, K. Mali, Fuzzy Electromagnetism Optimization (FEMO) and its application in biomedical image segmentation, Appl. Soft Comput. 97 (2020) 106800, http://dx.doi.org/10.1016/j.asoc.2020.106800.

[26] P. Zhang, Y. Zhong, Y. Deng, X. Tang, X. Li, CoSinGAN: Learning COVID-19 infection segmentation from a single radiological image, Diagnostics 10 (2020) 901, http://dx.doi.org/10.3390/diagnostics10110901.

[27] A. Oulefki, S. Agaian, T. Trongtirakul, A. Kassah Laouar, Automatic COVID-19 lung infected region segmentation and measurement using CT-scans images, Pattern Recognit. 114 (2020) 107747, http://dx.doi.org/10.1016/j.patcog.2020.107747.

[28] Q. Ni, Z.Y. Sun, L. Qi, W. Chen, Y. Yang, L. Wang, X. Zhang, L. Yang, Y. Fang, Z. Xing, Z. Zhou, Y. Yu, G.M. Lu, L.J. Zhang, A deep learning approach to characterize 2019 coronavirus disease (COVID-19) pneumonia in chest CT images, Eur. Radiol. 30 (2020) 6517–6527, http://dx.doi.org/10.1007/s00330-020-07044-9.

[29] T. Ozturk, M. Talo, E.A. Yildirim, U.B. Baloglu, O. Yildirim, U. Rajendra Acharya, Automated detection of COVID-19 cases using deep neural networks with X-ray images, Comput. Biol. Med. 121 (2020) 103792, http://dx.doi.org/10.1016/j.compbiomed.2020.103792.

[30] L. Li, L. Qin, Z. Xu, Y. Yin, X. Wang, B. Kong, J. Bai, Y. Lu, Z. Fang, Q. Song, K. Cao, D. Liu, G. Wang, Q. Xu, X. Fang, S. Zhang, J. Xia, J. Xia, Artificial intelligence distinguishes COVID-19 from community acquired pneumonia on chest CT, Radiology (2020) 200905, http://dx.doi.org/10.1148/radiol.2020200905.

[31] L. Huang, R. Han, T. Ai, P. Yu, H. Kang, Q. Tao, L. Xia, Serial quantitative chest CT assessment of COVID-19: A deep learning approach, Radiol. Cardiothorac. Imaging 2 (2020) e200075, http://dx.doi.org/10.1148/ryct.2020200075.

[32] K. Gao, J. Su, Z. Jiang, L.L. Zeng, Z. Feng, H. Shen, P. Rong, X. Xu, J. Qin, Y. Yang, W. Wang, D. Hu, Dual-branch combination network (DCN): Towards accurate diagnosis and lesion segmentation of COVID-19 using CT images, Med. Image Anal. 67 (2021) 101836, http://dx.doi.org/10.1016/j.media.2020.101836.

[33] T. Zheng, M. Oda, C. Wang, T. Moriya, Y. Hayashi, Y. Otake, M. Hashimoto, T. Akashi, M. Mori, H. Takabatake, H. Natori, K. Mori, Unsupervised segmentation of COVID-19 infected lung clinical CT volumes using image inpainting and representation learning, in: SPIE-Intl Soc Optical Eng, 2021, p. 120, http://dx.doi.org/10.1117/12.2580641.

[34] J. Singh, K. Gupta, Diagnosing Covid-19 using image processing and machine learning, Turkish J. Comput. Math. Educ. 12 (2021) 886–893, http://dx.doi.org/10.17762/TURCOMAT.V12I7.2672.

[35] S. Dash, S. Verma, Kavita, S. Bevinakoppa, M. Wozniak, J. Shafi, M.F. Ijaz, Guidance image-based enhanced matched filter with modified thresholding for blood vessel extraction, Symmetry 14 (2022) 194, http://dx.doi.org/10.3390/SYM14020194.

[36] M. Woźniak, J. Siłka, M. Wieczorek, Deep neural network correlation learning mechanism for CT brain tumor detection, Neural Comput. Appl. (2021) 1–16, http://dx.doi.org/10.1007/S00521-021-05841-X/FIGURES/17.

[37] L. li Guo, M. Woźniak, An image super-resolution reconstruction method with single frame character based on wavelet neural network in internet of things, Mob. Netw. Appl. 26 (2021) 390–403, http://dx.doi.org/10.1007/S11036-020-01681-6/FIGURES/13.

[38] M.M.A. Monshi, J. Poon, V. Chung, Deep learning in generating radiology reports: A survey, Artif. Intell. Med. 106 (2020) 101878, http://dx.doi.org/10.1016/j.artmed.2020.101878.

[39] A. Ulhaq, J. Born, A. Khan, D.P.S. Gomes, S. Chakraborty, M. Paul, COVID-19 control by computer vision approaches: A survey, IEEE Access 8 (2020) 179437–179456, http://dx.doi.org/10.1109/access.2020.3027685.

[40] J. Chen, L. Wu, J. Zhang, L. Zhang, D. Gong, Y. Zhao, S. Hu, Y. Wang, X. Hu, B. Zheng, K. Zhang, H. Wu, Z. Dong, Y. Xu, Y. Zhu, X. Chen, L. Yu, H. Yu, Deep learning-based model for detecting 2019 novel coronavirus pneumonia on high-resolution computed tomography: a prospective study, MedRxiv (2020) http://dx.doi.org/10.1101/2020.02.25.20021568, 2020.02.25.20021568.

[41] S. Wang, B. Kang, J. Ma, X. Zeng, M. Xiao, J. Guo, M. Cai, J. Yang, Y. Li, X. Meng, B. Xu, A deep learning algorithm using CT images to screen for Corona Virus Disease (COVID-19), MedRxiv (2020) http://dx.doi.org/10.1101/2020.02.14.20023028, 2020.02.14.20023028.

[42] C. Butt, J. Gill, D. Chun, B.A. Babu, Deep learning system to screen coronavirus disease 2019 pneumonia, Appl. Intell. (2020) 1, http://dx.doi.org/10.1007/s10489-020-01714-3.

[43] X. Xu, X. Jiang, C. Ma, P. Du, X. Li, S. Lv, L. Yu, Y. Chen, J. Su, G. Lang, Y. Li, H. Zhao, K. Xu, L. Ruan, W. Wu, Deep learning system to screen coronavirus disease 2019 pneumonia, Appl. Intell. 2019 (2020) 1–5, http://arxiv.org/abs/2002.09334 (accessed October 3, 2020).

[44] S. Jin, B. Wang, H. Xu, C. Luo, L. Wei, W. Zhao, X. Hou, W. Ma, Z. Xu, Z. Zheng, W. Sun, L. Lan, W. Zhang, X. Mu, C. Shi, Z. Wang, J. Lee, Z. Jin, M. Lin, H. Jin, L. Zhang, J. Guo, B. Zhao, Z. Ren, S. Wang, Z. You, J. Dong, X. Wang, J. Wang, W. Xu, AI-assisted CT imaging analysis for COVID-19 screening: Building and deploying a medical AI system in four weeks, MedRxiv (2020) http://dx.doi.org/10.1101/2020.03.19.20039354, 2020.03.19.20039354.

[45] X. Wang, X. Deng, Q. Fu, Q. Zhou, J. Feng, H. Ma, W. Liu, C. Zheng, A weakly-supervised framework for COVID-19 classification and lesion localization from chest CT, IEEE Trans. Med. Imaging 39 (2020) 2615–2625, http://dx.doi.org/10.1109/TMI.2020.2995965.

[46] A. Mohammed, C. Wang, M. Zhao, M. Ullah, R. Naseem, H. Wang, M. Pedersen, F.A. Cheikh, Weakly-supervised network for detection of COVID-19 in chest CT scans, IEEE Access 8 (2020) 155987–156000, http://dx.doi.org/10.1109/ACCESS.2020.3018498.

[47] I. Laradji, P. Rodriguez, O. Mañas, K. Lensink, M. Law, L. Kurzman, W. Parker, D. Vazquez, D. Nowrouzezahrai, A weakly supervised consistency-based learning method for COVID-19 segmentation in CT images, 2020, http://arxiv.org/abs/2007.02180 (accessed October 4, 2020).

[48] I. Laradji, P. Rodriguez, F. Branchaud-Charron, K. Lensink, P. Atighehchian, W. Parker, D. Vazquez, D. Nowrouzezahrai, A weakly supervised region-based active learning method for COVID-19 segmentation in CT images, 2020, http://arxiv.org/abs/2007.07012 (accessed October 4, 2020).

[49] O. Gozes, M. Frid-Adar, H. Greenspan, P.D. Browning, H. Zhang, W. Ji, A. Bernheim, E. Siegel, Rapid AI development cycle for the coronavirus (COVID-19) pandemic: Initial results for automated detection & patient monitoring using deep learning CT image analysis, 2020, http://arxiv.org/abs/2003.05037 (accessed October 4, 2020).

[50] S. Chakraborty, K. Mali, A morphology-based radiological image segmentation approach for efficient screening of COVID-19, Biomed. Signal Process. Control (2021) 102800, http://dx.doi.org/10.1016/j.bspc.2021.102800.

[51] C.H. Han, M. Kim, J.T. Kwak, Semi-supervised learning for an improved diagnosis of COVID-19 in CT images, PLoS One 16 (2021) e0249450, http://dx.doi.org/10.1371/journal.pone.0249450.

[52] Ş.I. Birbil, S.C. Fang, An electromagnetism-like mechanism for global optimization, J. Global Optim. 25 (2003) 263–282, http://dx.doi.org/10.1023/A:1022452626305.

[53] I. Tsamardinos, L.E. Brown, C.F. Aliferis, The max–min hill-climbing Bayesian network structure learning algorithm, Mach. Learn. 65 (2006) 31–78, http://dx.doi.org/10.1007/s10994-006-6889-7.

[54] S. ichi Amari, Backpropagation and stochastic gradient descent method, Neurocomputing 5 (1993) 185–196, http://dx.doi.org/10.1016/0925-2312(93)90006-O.

[55] F.A. Lindholm, J.G. Fossum, E.L. Burgess, Application of the superposition principle to solar-cell analysis, IEEE Trans. Electron Devices 26 (1979) 165–171, http://dx.doi.org/10.1109/T-ED.1979.19400.

[56] H. Sen Yan, X.Q. Wan, F.L. Xiong, A hybrid electromagnetism-like algorithm for two-stage assembly flow shop scheduling problem, Int. J. Prod. Res. 52 (2014) 5626–5639, http://dx.doi.org/10.1080/00207543.2014.894257.

[57] D. Oliva, E. Cuevas, G. Pajares, D. Zaldivar, Template matching using an improved electromagnetism-like algorithm, Appl. Intell. 41 (2014) 791–807, http://dx.doi.org/10.1007/s10489-014-0552-y.

[58] A.M. Turky, S. Abdullah, A multi-population electromagnetic algorithm for dynamic optimisation problems, Appl. Soft Comput. J. 22 (2014) 474–482, http://dx.doi.org/10.1016/j.asoc.2014.04.032.

[59] J.C. Bezdek, R. Ehrlich, W. Full, FCM: The fuzzy c-means clustering algorithm, Comput. Geosci. 10 (1984) 191–203, http://dx.doi.org/10.1016/0098-3004(84)90020-7.

[60] S. Chakraborty, K. Mali, SuFMoFPA: A superpixel and meta-heuristic based fuzzy image segmentation approach to explicate COVID-19 radiological images, Expert Syst. Appl. (2020) 114142, http://dx.doi.org/10.1016/j.eswa.2020.114142.

[61] O. Castillo, P. Melin, J. Kacprzyk, W. Pedrycz, Type-2 Fuzzy Logic: Theory and Applications, Institute of Electrical and Electronics Engineers (IEEE), 2008, p. 145, http://dx.doi.org/10.1109/grc.2007.118.

[62] O. Castillo, P. Melin, Optimization of type-2 fuzzy systems based on bio-inspired methods: A concise review, Inf. Sci. (Ny) 205 (2012) 1–19, http://dx.doi.org/10.1016/j.ins.2012.04.003.

[63] C. Qiu, J. Xiao, L. Yu, L. Han, M.N. Iqbal, A modified interval type-2 fuzzy C-means algorithm with application in MR image segmentation, Pattern Recognit. Lett. 34 (2013) 1329–1338, http://dx.doi.org/10.1016/j.patrec.2013.04.021.

[64] F.C.H. Rhee, Cheul Hwang, A type-2 fuzzy C-means clustering algorithm, in: Proc. Jt. 9th IFSA World Congr. 20th NAFIPS Int. Conf. (Cat. No. 01TH8569), IEEE, pp. 1926–1929, http://dx.doi.org/10.1109/NAFIPS.2001.944361.

[65] S. Chakraborty, K. Mali, Fuzzy modified cuckoo search for biomedical image segmentation, Knowl. Inf. Syst. 2022 (2022) 1–40, http://dx.doi.org/10.1007/S10115-022-01659-8.

[66] A.P. Moore, S.J.D. Prince, J. Warrell, U. Mohammed, G. Jones, Superpixel lattices, in: 26th IEEE Conf. Comput. Vis. Pattern Recognition, CVPR, 2008, http://dx.doi.org/10.1109/CVPR.2008.4587471.

[67] S. Chakraborty, K. Mali, A radiological image analysis framework for early screening of the COVID-19 infection: A computer vision-based approach, Appl. Soft Comput. 119 (2022) 108528, http://dx.doi.org/10.1016/J.ASOC.2022.108528.

[68] T.H. Kim, K.M. Lee, S.U. Lee, Learning full pairwise affinities for spectral segmentation, IEEE Trans. Pattern Anal. Mach. Intell. 35 (2013) 1690–1703, http://dx.doi.org/10.1109/TPAMI.2012.237.

[69] D. Comaniciu, P. Meer, Mean shift: A robust approach toward feature space analysis, IEEE Trans. Pattern Anal. Mach. Intell. 24 (2002) 603–619, http://dx.doi.org/10.1109/34.1000236.

[70] R. Achanta, A. Shaji, K. Smith, A. Lucchi, P. Fua, S. Süsstrunk, SLIC superpixels compared to state-of-the-art superpixel methods, IEEE Trans. Pattern Anal. Mach. Intell. 34 (2012) 2274–2281, http://dx.doi.org/10.1109/TPAMI.2012.120.

[71] Z. Hu, Q. Zou, Q. Li, Watershed superpixel, in: Proc. - Int. Conf. Image Process. ICIP, IEEE Computer Society, 2015, pp. 349–353, http://dx.doi.org/10.1109/ICIP.2015.7350818.

[72] S. Chakraborty, An advanced approach to detect edges of digital images for image segmentation, in: S. Chakraborty, K. Mali (Eds.), Appl. Adv. Mach. Intell. Comput. Vis. Object Recognit. Emerg. Res. Oppor., IGI GLobal, 2020, http://dx.doi.org/10.4018/978-1-7998-2736-8.ch004.

[73] S. Hore, S. Chakraborty, A.S. Ashour, N. Dey, A.S. Ashour, D. Sifaki-Pistolla, T. Bhattacharya, S.R.B. Chaudhuri, Finding contours of hippocampus brain cell using microscopic image analysis, J. Adv. Microsc. Res. 10 (2015) 93–103, http://dx.doi.org/10.1166/jamr.2015.1245.

[74] L. Vincent, Morphological grayscale reconstruction in image analysis: Applications and efficient algorithms, IEEE Trans. Image Process. 2 (1993) 176–201, http://dx.doi.org/10.1109/83.217222.

[75] S. Chen, R.M. Haralick, Recursive erosion, dilation, opening, and closing transforms, IEEE Trans. Image Process. 4 (1995) 335–345, http://dx.doi.org/10.1109/83.366481.

[76] S. Chakraborty, M. Roy, S. Hore, A study on different edge detection techniques in digital image processing, 2018, http://dx.doi.org/10.4018/978-1-5225-5204-8.ch070.

[77] W. Ding, S. Chakraborty, K. Mali, S. Chatterjee, J. Nayak, A.K. Das, S. Banerjee, An unsupervised fuzzy clustering approach for early screening of COVID-19 from radiological images, IEEE Trans. Fuzzy Syst. (2021) 1, http://dx.doi.org/10.1109/TFUZZ.2021.3097806.

[78] COVID-19: caso 47 | SIRM, 2020, https://www.sirm.org/2020/03/14/covid-19-caso-47/ (accessed May 5, 2020).

[79] Covid-19_CTscans/metadata.csv at master · bjmcshane/Covid-19_CTscans · GitHub, 2022, https://github.com/bjmcshane/Covid-19_CTscans/blob/master/metadata.csv (accessed April 25, 2022).

[80] M. Hollett, D. Bell, COVID-19, Radiopaedia.Org, 2020, http://dx.doi.org/10.53347/RID-73913.

[81] Case 009-64 year old, female | Coronavirus Cases - 冠状病毒病例, 2020, https://coronacases.org/forum/coronacases-org-helping-radiologists-to-help-people-in-more-than-100-countries-1/question/case-009-64-year-old-female-16 (accessed May 16, 2020).

[82] Case 010-55 year old, female | Coronavirus Cases - 冠状病毒病例, 2020, https://coronacases.org/forum/coronacases-org-helping-radiologists-to-help-people-in-more-than-100-countries-1/question/case-010-55-year-old-female-15 (accessed May 16, 2020).

[83] S.C. Cheng, Y.C. Chang, Y.L. Fan Chiang, Y.C. Chien, M. Cheng, C.H. Yang, C.H. Huang, Y.N. Hsu, First case of coronavirus disease 2019 (COVID-19) pneumonia in Taiwan, J. Formos. Med. Assoc. 119 (2020) 747–751, http://dx.doi.org/10.1016/j.jfma.2020.02.007.

[84] COVID-19 pneumonia | Radiology Case | Radiopaedia.org, 2020, https://radiopaedia.org/cases/covid-19-pneumonia-7 (accessed April 23, 2020).

[85] COVID-19 pneumonia | Radiology Case | Radiopaedia.org, 2020, https://radiopaedia.org/cases/covid-19-pneumonia-14 (accessed May 6, 2020).

[86] J. Lim, S. Jeon, H.Y. Shin, M.J. Kim, Y.M. Seong, W.J. Lee, K.W. Choe, Y.M. Kang, B. Lee, S.J. Park, Case of the index patient who caused tertiary transmission of coronavirus disease 2019 in Korea: The application of lopinavir/ritonavir for the treatment of COVID-19 pneumonia monitored by quantitative RT-PCR, J. Korean Med. Sci. 35 (2020) http://dx.doi.org/10.3346/jkms.2020.35.e79.

[87] COVID-19: caso 14 | SIRM, 2020, https://www.sirm.org/2020/03/08/covid-19-caso-14/ (accessed May 16, 2020).

[88] COVID-19: case 4 | SIRM, 2020, https://www.sirm.org/2020/03/04/covid-19-caso-4/ (accessed April 18, 2020).

[89] COVID-19 pneumonia | Radiology Case | Radiopaedia.org, 2020, https://radiopaedia.org/cases/covid-19-pneumonia-4 (accessed May 16, 2020).

[90] Normal CT chest | Radiology Case | Radiopaedia.org, 2021, https://radiopaedia.org/cases/normal-ct-chest (accessed March 5, 2021).

[91] D.L. Davies, D.W. Bouldin, A cluster separation measure, IEEE Trans. Pattern Anal. Mach. Intell. PAMI-1 (1979) 224–227, http://dx.doi.org/10.1109/TPAMI.1979.4766909.

[92] X.L. Xie, G. Beni, A validity measure for fuzzy clustering, IEEE Trans. Pattern Anal. Mach. Intell. 13 (1991) 841–847, http://dx.doi.org/10.1109/34.85677.

[93] J.C. Dunn, Well-separated clusters and optimal fuzzy partitions, J. Cybern. 4 (1974) 95–104, http://dx.doi.org/10.1080/01969727408546059.

[94] S.K. Pal, A. Ghosh, B.U. Shankar, Segmentation of remotely sensed images with fuzzy thresholding, and quantitative evaluation, Int. J. Remote Sens. 21 (2000) 2269–2300, http://dx.doi.org/10.1080/01431160050029567.

[95] C. Blum, Beam-ACO - Hybridizing ant colony optimization with beam search: An application to open shop scheduling, Comput. Oper. Res. 32 (2005) 1565–1591, http://dx.doi.org/10.1016/j.cor.2003.11.018.

[96] M. Taherkhani, R. Safabakhsh, A novel stability-based adaptive inertia weight for particle swarm optimization, Appl. Soft Comput. J. 38 (2016) 281–295, http://dx.doi.org/10.1016/j.asoc.2015.10.004.

[97] R.L. Kadri, F.F. Boctor, An efficient genetic algorithm to solve the resource-constrained project scheduling problem with transfer times: The single mode case, European J. Oper. Res. 265 (2018) 454–462, http://dx.doi.org/10.1016/j.ejor.2017.07.027.

[98] S. Chakraborty, S. Chatterjee, N. Dey, A.S. Ashour, A.S. Ashour, F. Shi, K. Mali, Modified cuckoo search algorithm in microscopic image segmentation of hippocampus, Microsc. Res. Tech. (2017) 1–22, http://dx.doi.org/10.1002/jemt.22900.

[99] E. Rodríguez-Esparza, L.A. Zanella-Calzada, D. Oliva, A.A. Heidari, D. Zaldivar, M. Pérez-Cisneros, L.K. Foong, An efficient Harris hawks-inspired image segmentation method, Expert Syst. Appl. 155 (2020) 113428, http://dx.doi.org/10.1016/J.ESWA.2020.113428.

[100] S. Kapoor, I. Zeya, C. Singhal, S.J. Nanda, A grey wolf optimizer based automatic clustering algorithm for satellite image segmentation, Procedia Comput. Sci. 115 (2017) 415–422, http://dx.doi.org/10.1016/J.PROCS.2017.09.100.

[101] S. Tongbram, B.A. Shimray, L.S. Singh, N. Dhanachandra, A novel image segmentation approach using fcm and whale optimization algorithm, J. Ambient Intell. Humaniz. Comput. 2021 (2021) 1–15, http://dx.doi.org/10.1007/S12652-020-02762-W.

[102] Z.K. Eisham, M.M. Haque, M.S. Rahman, M.M. Nishat, F. Faisal, M.R. Islam, Chimp optimization algorithm in multilevel image thresholding and image clustering, Evol. Syst. 2022 (2022) 1–44, http://dx.doi.org/10.1007/S12530-022-09443-3.

[103] J. Zhao, D. Yu, A new approach for multilevel image segmentation based on fuzzy cellular neural network, J. Electron. 17 (2000) 46–52, http://dx.doi.org/10.1007/S11767-000-0021-0, 171.

[104] S. Chakraborty, S. Bhowmik, An efficient approach to job shop scheduling problem using simulated annealing, Int. J. Hybrid Inf. Technol. 8 (2015) 273–284, http://dx.doi.org/10.14257/ijhit.2015.8.11.23.

[105] S. Mahdavi, M.E. Shiri, S. Rahnamayan, Metaheuristics in large-scale global continues optimization: A survey, Inf. Sci. (Ny) 295 (2015) 407–428, http://dx.doi.org/10.1016/j.ins.2014.10.042.

[106] B. Brekhna, A. Mahmood, Y. Zhou, Robustness analysis of superpixel algorithms to image blur, additive Gaussian noise, and impulse noise, J. Electron. Imaging 26 (2017) 1, http://dx.doi.org/10.1117/1.jei.26.6.061604.

[107] L. Li, L. Sun, J. Guo, C. Han, S. Li, Fuzzy multilevel image thresholding based on modified quick artificial bee colony algorithm and local information aggregation, Math. Probl. Eng. 2016 (2016) http://dx.doi.org/10.1155/2016/5985616.